The Astrophysical Journal Supplement Series, 284:77 (17pp), 2026 June https://doi.org/10.3847/1538-4365/ae632f
© 2026. The Author(s). Published by the American Astronomical Society.
OPEN ACCESS

FAST Polarization Catalog of FRB 20240114A

Tian-Cong Wang[1,2,38], Jun-Shuo Zhang[3,4,38], Xiao-Hui Liu[3,4,38], Wei-Yang Wang[4], Pei Wang[2,3,5], He Gao[1,2], Di Li[3,5,6], Bing Zhang[7,8,9,10], Wei-Wei Zhu[2,3,5], Jin-Lin Han[3,4,5], Ke-Jia Lee[3,11,12,13], Ye Li[14], Dengke Zhou[15], Wan-Jin Lu[3,4], Jintao Xie[16], Jianhua Fang[15], Jin-Huang Cao[3,4], Chen-Chen Miao[17], Yu-Hao Zhu[3,4], Yunchuan Chen[15], Si-Lu Xu[3,4], Huaxi Chen[15], Xiao-Feng Cheng[15], Qin Wu[18], Shuo Cao[4,12], Long-Xuan Zhang[19], Shi-Yan Tian[19], Yong-Kun Zhang[3], Yi Feng[15,20], De-Jiang Zhou[3], Jia-Rui Niu[3], Heng Xu[3], Xuelei Chen[4,5], Yuan-Pei Yang[21], Dong-Zi Li[22,23], Fa-Yin Wang[18,24], Chao-Wei Tsai[2,3,4,5], Wen-Fei Yu[25], Chen-Hui Niu[26], Jia-Wei Luo[27,28], Rui Luo[29], E. Güngercinoğlu[30], Zi-Wei Wu[3], Chun-Feng Zhang[3], Xiang-Lei Chen[3], Shuai Feng[3,4], Xiang-Han Cui[3,31], Qing-Yue Qu[3,4], Yuan-Hong Qu[9,10], Bo-Jun Wang[3], Yi-Dan Wang[3,4], Lin Lin[1], Ai-Yuan Yang[3,5], Yuan-Chuan Zou[14,19], Yu-Xiang Huang[12], Wei-Cong Jing[3], Jian Li[32,33], Yong-Feng Huang[18,24], Su-Ming Weng[34,35], Shi-Han Yew[34,35], Xue-Feng Wu[14], Lei Zhang[3,36], and Ru-Shuang Zhao[37]

[1] School of Physics and Astronomy, Beijing Normal University, Beijing 100875, People's Republic of China; gaohe@bnu.edu.cn
[2] Institute for Frontiers in Astronomy and Astrophysics, Beijing Normal University, Beijing 102206, People's Republic of China; wangpei@nao.cas.cn
[3] National Astronomical Observatories, Chinese Academy of Sciences, Beijing 100101, People's Republic of China; dili@tsinghua.edu.cn
[4] University of Chinese Academy of Sciences, Beijing 100049, People's Republic of China
[5] State Key Laboratory of Radio Astronomy and Technology, Beijing 100101, People's Republic of China
[6] New Cornerstone Science Laboratory, Department of Astronomy, Tsinghua University, Beijing 100084, People's Republic of China
[7] The Hong Kong Institute for Astronomy and Astrophysics, the University of Hong Kong, Pokfulam, Hong Kong, People's Republic of China; bzhang1@hku.hk
[8] Department of Physics, the University of Hong Kong, Pokfulam, Hong Kong, People's Republic of China
[9] Nevada Center for Astrophysics, University of Nevada, Las Vegas, NV 89154, USA
[10] Department of Physics and Astronomy, University of Nevada Las Vegas, Las Vegas, NV 89154, USA
[11] Department of Astronomy, School of Physics, Peking University, Beijing 100871, People's Republic of China
[12] Yunnan Astronomical Observatories, Chinese Academy of Sciences, Kunming 650216, People's Republic of China
[13] Beijing Laser Acceleration Innovation Center, Huairou, Beijing 101400, People's Republic of China
[14] Purple Mountain Observatory, Chinese Academy of Sciences, Nanjing 210023, People's Republic of China
[15] Research Center for Astronomical Computing, Zhejiang Laboratory, Hangzhou 311121, People's Republic of China
[16] School of Computer Science and Engineering, Sichuan University of Science and Engineering, Yibin 644000, People's Republic of China
[17] College of Physics and Electronic Engineering, Qilu Normal University, Jinan 250200, People's Republic of China
[18] School of Astronomy and Space Science, Nanjing University, Nanjing 210023, People's Republic of China
[19] School of Physics, Huazhong University of Science and Technology, Wuhan, 430074, People's Republic of China
[20] Institute for Astronomy, School of Physics, Zhejiang University, Hangzhou 310027, People's Republic of China
[21] South-Western Institute for Astronomy Research, Key Laboratory of Survey Science of Yunnan Province, Yunnan University, Kunming 650500, People's Republic of China
[22] Department of Astrophysical Sciences, Princeton University, Princeton, NJ 89154, USA
[23] Department of Astronomy, Tsinghua University, Beijing 100084, People's Republic of China
[24] Key Laboratory of Modern Astronomy and Astrophysics (Nanjing University), Ministry of Education, Nanjing 210093, People's Republic of China
[25] Shanghai Astronomical Observatory, Chinese Academy of Sciences, Shanghai 200030, People's Republic of China
[26] Institute of Astrophysics, Central China Normal University, Wuhan 430079, People's Republic of China
[27] College of Physics and Hebei Key Laboratory of Photophysics Research and Application, Hebei Normal University, Shijiazhuang 050024, People's Republic of China
[28] Shijiazhuang Key Laboratory of Astronomy and Space Science, Hebei Normal University, Shijiazhuang 050024, People's Republic of China
[29] Department of Astronomy, School of Physics and Materials Science, Guangzhou University, Guangzhou 510006, People's Republic of China
[30] School of Arts and Sciences, Qingdao Binhai University, Qingdao 266555, People's Republic of China
[31] The Netherlands Institute for Radio Astronomy, Oude Hoogeveensedijk 4,7991 PD Dwingeloo, The Netherlands
[32] Department of Astronomy, University of Science and Technology of China, Hefei 230026, People's Republic of China
[33] School of Astronomy and Space Science, University of Science and Technology of China, Hefei 230026, People's Republic of China
[34] National Key Laboratory of Dark Matter Physics, School of Physics and Astronomy, Shanghai Jiao Tong University, Shanghai 200240, People's Republic of China
[35] Laboratory for Laser Plasmas and Collaborative Innovation Centre of IFSA, Shanghai Jiao Tong University, Shanghai 200240, People's Republic of China
[36] Centre for Astrophysics and Supercomputing, Swinburne University of Technology, Hawthorn, VIC 3122, Australia
[37] Guizhou Provincial Key Laboratory of Radio Astronomy and Data Processing, Guizhou Normal University, Guiyang 550001, People's Republic of China
Received 2026 March 12; revised 2026 April 16; accepted 2026 April 17; published 2026 June 9

Abstract

Polarization measurements of fast radio bursts (FRBs) probe the magnetized plasma surrounding their central engines. FRB 20240114A is an exceptionally active repeating source, with 17,356 bursts detected between 2024 January 28 and 2025 May 30 by FAST, enabling studies of the temporal evolution of its polarization properties. In this work, we present a polarimetric catalog of 6131 bright bursts (with a signal-to-noise ratio (S/N) $\geqslant 20$, 35.3% of the total sample), including arrival time (MJD_{topo}), dispersion measure (DM), burst width (W_{eff}), bandwidth,

[38] These authors contributed equally to this work.

Original content from this work may be used under the terms of the Creative Commons Attribution 4.0 licence. Any further distribution of this work must maintain attribution to the author(s) and the title of the work, journal citation and DOI.

Faraday rotation measure (RM), linear and circular polarization degrees (L/I, V/I), and intrinsic polarization angle (PA_0). We confirm a clear temporal evolution of RM: after an initial stable phase, it decreases linearly by $\sim$200 rad m^{-2} over 200 days, forming a bimodal distribution, whereas DM remains stable at 529.3 $\pm$ 1.2 pc cm^{-3}. The linear polarization fraction is generally high, with the 3σ lower bound around 76%, while circular polarization is low, with 1157 of 17,356 bursts (6.67%) having $|V|/I \geqslant 10\%$. We perform a power-law fit between $|V|/I$ and |RM|, which yields an index of -2.98 ± 0.80. It is found that the combined 2D distribution of L/I versus V/I remains stable, implying that the emission mechanism is largely invariant. Our PA_0 measurements show a broad, nonuniform distribution, implying a complex emission geometry. These results suggest that FRB 20240114A resides in a dynamically evolving magneto-ionic environment. This catalog provides a foundation for studies of repeating FRB progenitors and their environments.

Unified Astronomy Thesaurus concepts: High energy astrophysics (739); Radio transient sources (2008); Polarimetry (1278); Catalogs (205)

Materials only available in the online version of record: machine-readable table

1. Introduction

Fast radio bursts (FRBs) represent one of the most energetic and enigmatic phenomena in the transient Universe (B. Zhang 2023). Since their discovery (D. R. Lorimer et al. 2007; D. Thornton et al. 2013), the identification of repeating sources (L. G. Spitler et al. 2016; CHIME/FRB Collaboration et al. 2019) has provided a crucial path toward understanding their progenitors. Among the various observational tools, radio polarimetry has proven to be exceptionally powerful. Measurements of the linear polarization and the Faraday rotation measure (RM) offer a direct probe into the magneto-ionic environment surrounding the FRB source, potentially revealing the presence of a supernova remnant (SNR), a pulsar wind nebula, or a binary companion's wind (D. Michilli et al. 2018; Y.-P. Yang et al. 2020; F. Y. Wang et al. 2022; Y. Qu & B. Zhang 2023). Furthermore, the temporal evolution of these properties can shed light on the dynamics of this local environment (G. H. Hilmarsson et al. 2021; H. Xu et al. 2022).

While individual case studies of bright bursts are valuable, a comprehensive statistical understanding of an FRB's behavior requires large, uniform samples of bursts observed with a single, stable instrument. Such datasets mitigate instrumental biases and allow for the robust investigation of burst-to-burst variations, energy distributions, and long-term temporal evolution.

Recent years have also seen the emergence of systematic FRB polarization catalogs from multiple instruments. For nonrepeating FRBs, polarimetric catalogs have been presented for samples detected with DSA-110 (M. B. Sherman et al. 2024), the Canadian Hydrogen Intensity Mapping Experiment (CHIME)/FRB (A. Pandhi et al. 2024), and ASKAP (D. R. Scott et al. 2025). For repeating sources, recent CHIME/FRB studies have established the largest source-level polarization catalogs to date (R. Mckinven et al. 2023a; C. Ng et al. 2025), enabling comparative studies across repeater populations. In this context, the present work is complementary: rather than a source-level census, we provide a large burst-level, time-resolved polarization catalog for a single exceptionally active repeating FRB, making it possible to investigate burst-to-burst variations and long-term temporal evolution within one source.

The repeating FRB 20240114A, discovered shortly after its initial activity, has established itself as one of the most prolific known sources (J. Tian et al. 2024; U. Panda et al. 2025; J.-T. Xie et al. 2025; J.-S. Zhang et al. 2025; L.-X. Zhang et al. 2025; K. Shin et al. 2026; D. Zhou et al. 2026). Its sustained high burst rate over an extended period makes it an ideal target for amassing a large catalog of bursts. The Five-hundred-meter Aperture Spherical radio Telescope (FAST; R. Nan et al. 2011), with its unparalleled sensitivity, is uniquely capable of detecting the faint end of the burst energy distribution with a fluence completeness threshold of 0.026 Jy ms from such a source (J.-S. Zhang et al. 2025), thereby providing a complete and unbiased sample. This extreme sensitivity also makes FAST a powerful platform for high-precision polarimetry. Previous FAST observations have revealed diverse polarization-angle swings, frequency-dependent polarization behavior, extreme circular polarization, and temporal evolution of the local magneto-ionic environment in repeating FRBs (R. Luo et al. 2020; J.-C. Jiang et al. 2022; H. Xu et al. 2022; R. Anna-Thomas et al. 2023; J. C. Jiang et al. 2024; J. R. Niu et al. 2024; Y. Feng et al. 2025; D. Zhou et al. 2025; Y. Li et al. 2026), demonstrating that polarimetric measurements can serve as a sensitive probe of their extreme and dynamic environments. Building on these results, the present work provides a systematic polarimetric catalog and time-resolved statistical analysis of FRB 20240114A based on a much larger burst sample.

This paper is the first in a series devoted to unveiling the polarization nature of FRB 20240114A through FAST observations. Herein, we focus exclusively on the presentation and public release of the polarization catalog. We describe our 16 month observations from 2024 to 2025, the detailed data reduction pipeline, and the calibration procedures that underpin this dataset. The resulting catalog comprises over 6000 bursts, each with measured time of arrival (TOA), dispersion measure (DM), RM, and linear and circular polarization fractions.

We explicitly state that the comprehensive scientific analysis of this catalog, including the search for periodicity, the detailed modeling of RM evolution, and the investigation of burst subpopulations, will be the focus of subsequent publications in this series. The purpose of this paper is to establish the data product itself, ensuring its reliability and making it available to the broader community for independent analysis.

This paper is organized as follows. In Section 2, we describe the FAST observations and the data processing procedures, including burst search and parameter measurements. The catalog of bursts is presented in Section 3, providing a detailed description of the catalog. In Section 4, we analyze the data quality and global properties of the bursts, including parameter distributions and correlations. Section 5 is dedicated to a

discussion of the possible origins of the RM evolution and the complex and variable geometry of the emission region. Finally, a summary and information on data access are provided in Section 6.

2. Observations and Data Processing

2.1. FAST Observations and Burst Search

An observation campaign of FRB 20240114A was conducted using the FAST telescope for over 16 months, from 2024 January 28 to 2025 May 30. The initial observations employed the position reported by CHIME (K. Shin et al. 2026; R.A. = $21^{h}27^{m}39\overset{s}{.}888$, decl. = $+04°21'0\overset{''}{.}36$). Starting from 2024 February 15 (UT), the pointing was updated to the refined location (R.A. = $21^{h}27^{m}39\overset{s}{.}84$, decl. = $+04°19'46\overset{''}{.}3$) localized by MeerKAT (J. Tian et al. 2024). The observing campaign comprised 97 sessions, totaling 57.99 hr of exposure time. Observations covered the 1.0–1.5 GHz band using the central beam of the 19-beam receiver in tracking mode. Most data were recorded in the 8 bit PSRFITS format, providing full Stokes polarization information, 4096 frequency channels with a frequency resolution of 0.1221 MHz, and a time resolution of 49.152 μs.

We performed single-pulse searches on the FAST data using the PRESTO software package (S. M. Ransom 2001), which employs a matched-filtering technique that applies boxcar functions of varying widths to the dedispersed time series to identify pulses across a range of timescales. The pipeline was described in P. Wang et al. (2025). To evaluate the completeness of the burst search, we also cross-checked the PRESTO results using two additional search approaches: DRAFTS, a deep-learning-based radio fast transient search pipeline (Y.-K. Zhang et al. 2025), and the AI-aided pipeline described in P. Wang et al. (2024). In the present work, PRESTO serves as the primary burst-search pipeline, while these two methods are used as auxiliary cross-verification tools rather than as independent parallel catalog-building pipelines. By comparing their candidate lists with the PRESTO detections on the same dataset, we verified that there is no obvious population of missed bursts in the final sample. This process identified 17,356 bursts exceeding our detection threshold, defined by a fluence signal-to-noise ratio (S/N) of $S/N_f \geqslant 12$, where S/N_f denotes the S/N of the burst fluence, i.e., the integrated burst flux over its duration, rather than the peak-flux S/N (see J.-S. Zhang et al. 2025). From this sample, we selected 6384 bursts with $S/N \geqslant 20$ for polarization analysis.

2.2. Parameter Measurement

The TOA for each burst was determined by measuring the time at which the cumulative fluence reached 50% of its total value, following the burst identification criteria defined in D. Li et al. (2021) and L.-X. Zhang et al. (2025), which classify multiple pulses as components of a single burst when a complex time-frequency structure is bridged by emission above 5σ. The final TOA is taken as the topocentric arrival time (MJD) at the 1.5 GHz reference. For the polarization analysis, the effective temporal limits of each burst are defined by its measured TOA and full width at half-maximum (FWHM), adopting a time window of TOA $\pm$ 1.5 $\times$ FWHM. The FWHM is obtained by fitting a Gaussian to the autocorrelation function of the same profile.

The DM of each burst was refined using the DM-power package (H.-H. Lin et al. 2022). Unlike the traditional approach of maximizing the peak S/N of the frequency-summed profile, which can be biased by complex subburst drifting and frequency-dependent morphology, DM-power optimizes the DM in the Fourier domain. The method decomposes the dynamic spectrum into Fourier components along the time axis and measures the DM independently at different Doppler (Fourier) frequencies. Since short-timescale structures are more sensitive to residual dispersive delays, the algorithm effectively weights information across multiple timescales, yielding a more robust and high-precision DM measurement.

For bursts exhibiting ambiguous morphology in the dynamic spectrum or relatively low S/N, the multicomponent optimization may become unstable and lead to overfitting. In such cases, we adopt the daily averaged DM values to ensure consistency across the sample. The derived DMs have a median value of 529.3 pc cm^{-3} with a standard deviation of 1.2 pc cm^{-3}, consistent with the measurement reported by CHIME/FRB (K. Shin et al. 2026).

The burst frequency boundaries were determined using the cumulative distribution function (CDF)-based method proposed by J.-T. Xie et al. (2025). For each burst, the spectrum was first constructed by integrating the on-pulse flux density over time for each frequency channel. The CDF of the spectrum was then calculated and smoothed using the asymmetrically reweighted penalized least squares (arPLS) algorithm to suppress noise fluctuations. The lower and upper frequency limits were defined as the frequencies where the first derivative of the normalized CDF rises above and subsequently falls below thresholds determined by the S/N, specifically $1/(S/N)$ for the rising edge and $1-1/(S/N)$ for the falling edge. This procedure identifies the dominant emission band based on significant spectral power gradients rather than assuming a Gaussian spectral shape, and is therefore not equivalent to Gaussian fitting.

For bursts truncated by the observational band edges, a Gaussian extrapolation was applied to estimate the intrinsic bandwidth (BW). For bursts with complex spectral morphologies or insufficient S/N for a reliable boundary identification, a boxcar BW was adopted as a conservative estimate.

We applied the RM synthesis method to all 6384 bursts with $S/N \geqslant 20$, searching for RMs over the range from -2000 to 2000 rad m^{-2} (M. A. Brentjens & A. G. de Bruyn 2005). The adopted range was chosen as a conservative symmetric interval, comfortably wider than the RMs actually measured for FRB 20240114A. For the present FAST *L*-band channelization, intrachannel depolarization would become important only at much larger |RM|, and therefore does not limit the current RM measurements. To ensure data reliability, we examined each burst for potential saturation effects in the FAST receiver. By inspecting the four polarization components (XX, YY, $X^{*}Y$, $Y^{*}X$) and identifying data points at the critical thresholds, we flagged and subsequently excluded bursts exhibiting genuine saturation signatures. This screening removed 253 bursts from the initial sample with $S/N \geqslant 20$, leaving a final sample of 6131 nonsaturated bursts with reliable RM measurements for the polarization analysis (see Appendix A for details).

The observed RMs include a contribution from the Earth's ionosphere, which adds a time-variable component to the intrinsic RM. Using the IonFR Python code and global ionospheric map (GIM) products (C. Sotomayor-Beltran et al. 2013), we

Table 1
Description of the Catalog Columns

Column Name	Unit	Description
Burst ID	…	A unique identifier for each burst (which is consistent with J.-S. Zhang et al. 2025).
MJD_{topo}	day	Topocentric arrival time (MJD) at the 1.5 GHz reference.
DM	pc cm^{-3}	Best-fit dispersion measure by DM-power.
W_{eff}	ms	Full width at half-maximum (FWHM) of the burst.
Bandwidth	MHz	The frequency bandwidth of the burst.
RM	rad m^{-2}	Rotation measure determined via RM synthesis.
L/I	%	Debiased linear polarization fraction.
V/I	%	Circular polarization fraction.
PA_0	deg	The intrinsic polarization position angle at the infinite-frequency reference, corrected for RM.
S/N	…	Signal-to-noise ratio of the burst in the total intensity profile.

Table 2
Sample Table of Burst Parameters for FRB 20240114A with S/N $\geqslant$ 20

Burst ID	MJD_{topo}	DM (pc cm^{-3})	RM (rad m^{-2})	L/I (%)	V/I (%)	W_{eff} (ms)	Bandwidth (MHz)	PA_0 (deg)	S/N
B00001	60337.23827975	529.5 ± 0.1	$328.5^{+1.6}_{-1.6}$	96.3 ± 2.1	-7.1 ± 1.5	3.51 ± 0.23	188.3 ± 10.6	-7.8	29.7
B00007	60337.25012753	527.7 ± 0.1	$317.5^{+1.7}_{-1.7}$	97.3 ± 2.8	-12.3 ± 2.0	3.02 ± 0.21	207.7 ± 6.2	46.3	38.3
B00009	60338.21737789	528.5 ± 0.1	$326.5^{+2.8}_{-2.9}$	97.1 ± 3.1	-26.1 ± 2.3	1.62 ± 0.06	319.2 ± 8.1	19.0	46.9
B00011	60338.22518088	527.2 ± 0.6	$335.5^{+6.4}_{-5.3}$	60.4 ± 3.8	-82.4 ± 4.2	2.52 ± 0.14	74.5 ± 6.7	7.3	20.4
B00012	60338.22802442	528.3 ± 0.1	$330.5^{+2.2}_{-2.1}$	98.8 ± 2.1	1.0 ± 1.5	2.0 ± 0.07	158.7 ± 21.2	73.1	42.8
B00018	60338.23511480	531.1 ± 0.6	$330.5^{+1.9}_{-1.9}$	102.3 ± 2.8	-11.6 ± 1.9	3.96 ± 0.2	155.5 ± 4.0	11.8	22.0
B00019	60338.23556485	529.1 ± 0.1	$327.5^{+2.2}_{-2.3}$	92.1 ± 2.6	-0.7 ± 1.9	2.47 ± 0.1	174.1 ± 21.5	8.7	33.0
B00028	60341.19895450	530.4 ± 0.5	$343.5^{+2.4}_{-2.3}$	54.6 ± 2.5	11.2 ± 2.2	3.65 ± 0.2	121.3 ± 6.6	-53.4	20.5
B00031	60349.15748811	529.0 ± 0.3	$348.5^{+2.6}_{-2.7}$	98.4 ± 1.8	18.4 ± 1.3	1.94 ± 0.09	90.2 ± 14.3	-48.8	28.8
B00032	60349.15783813	528.5 ± 0.1	$350.5^{+0.7}_{-0.7}$	96.1 ± 1.2	-6.5 ± 0.9	4.91 ± 0.16	237.6 ± 9.4	23.6	34.6
B17290	60824.89193507	530.9 ± 0.1	$246.1^{+1.0}_{-1.1}$	99.3 ± 2.2	-5.1 ± 1.5	3.09 ± 0.02	276.4 ± 5.9	7.4	56.0
B17310	60824.89230168	530.0 ± 0.1	$231.9^{+7.0}_{-5.1}$	86.3 ± 9.4	1.8 ± 7.1	2.81 ± 0.03	325.1 ± 12.6	52.6	57.4
B17313	60824.89238065	529.8 ± 0.1	$250.7^{+1.3}_{-1.3}$	99.2 ± 2.2	-10.8 ± 1.6	1.98 ± 0.01	458.9 ± 9.4	-50.2	152.0
B17315	60824.89327416	529.6 ± 0.2	$248.1^{+1.4}_{-1.7}$	103.8 ± 3.0	1.4 ± 2.1	3.99 ± 0.02	442.5 ± 14.7	-11.2	54.7
B17317	60824.89356171	530.2 ± 0.1	$242.7^{+1.0}_{-0.9}$	91.5 ± 1.9	-22.9 ± 1.5	3.04 ± 0.03	204.1 ± 10.3	35.1	53.6
B17318	60824.89386021	529.8 ± 0.1	$245.3^{+0.4}_{-0.4}$	97.7 ± 0.7	9.9 ± 0.5	3.65 ± 0.01	255.5 ± 8.8	59.2	177.9
B17328	60824.89416654	529.4 ± 0.2	$243.5^{+0.7}_{-0.7}$	100.2 ± 1.5	-2.9 ± 1.0	2.55 ± 0.02	195.6 ± 6.7	-64.3	106.0
B17332	60824.89625329	530.6 ± 0.1	$240.1^{+4.5}_{-4.0}$	90.9 ± 8.7	16.1 ± 6.5	2.19 ± 0.07	287.8 ± 4.2	11.0	26.4
B17344	60824.89625000	530.5 ± 0.1	$239.5^{+1.4}_{-1.3}$	94.4 ± 4.7	0.9 ± 3.4	2.12 ± 0.05	213.0 ± 8.6	33.1	40.8

Note. All uncertainties in this table are rounded to one decimal place, following J.-S. Zhang et al. (2025) for consistency with previously published results. For a small subset of bursts whose DM uncertainties would be rounded to 0.0 under this convention, we uniformly adopt a conservative floor value of 0.1 pc cm^{-3} to avoid reporting unphysical zero-valued uncertainties. The quoted RM uncertainties are empirical estimates based on the RM-synthesis peak width and burst S/N. An additional systematic uncertainty comparable to one RM-search grid step ($\sim$ 0.2 rad m^{-2}) may also be considered.

(This table is available in its entirety in machine-readable form in the online article.)

calculated the ionospheric RM for each observing session and corrected the RM values (see Appendix C for details).

We additionally conducted a systematic search for Faraday conversion across all bursts. Faraday conversion is a propagation effect in a magnetized plasma with a perpendicular magnetic field, converting linear polarization into circular polarization. Combined with Faraday rotation, if the Faraday conversion is observed, the detection would constrain plasma properties and magnetic field geometry along the line of sight (W.-Y. Wang et al. 2025). Our analysis found no significant evidence of conversion in any of the bursts in our sample, consistent with the results of P. A. Uttarkar et al. (2026a), indicating that the observed circular polarization is likely intrinsic to the emission mechanism rather than being generated by propagation effects.

3. The Catalog Description

The primary product of this work is a machine-readable catalog containing the measured parameters for the 6131 bursts detected from FRB 20240114A. The catalog is structured as a table, with each row representing a single burst and each column a specific measured parameter, and the detailed description of the catalog columns is presented in Table 1. An abridged version of the catalog is presented in Table 2 for illustration. The full catalog is available online in CSV formats.

For the convenience of catalog users, we also provide estimates of the Galactic foreground contributions toward FRB 20240114A. Using the YMW16 and NE2025 Galactic electron-density models (J. M. Yao et al. 2017; S. K. Ocker & J. M. Cordes 2026), we obtain Galactic interstellar DMs of $DM_{MW,ISM} = 38.82 \pm 4.78$ pc cm^{-3} and 51.05 ± 7.45 pc cm^{-3},

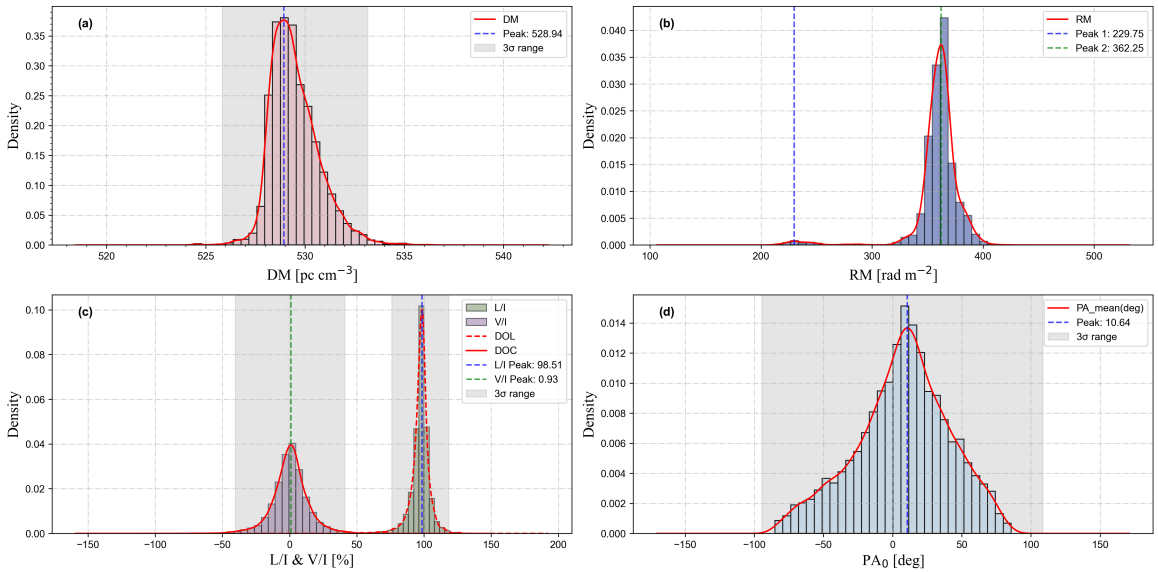


Figure 1. Distributions of key parameters for the 6131 bursts from FRB 20240114A. (a) DM. The distribution is narrow and peaks near 528.9 pc cm^{-3}. (b) RM. The distribution shows a complex, non-Gaussian shape with a primary peak near 362.2 rad m^{-2} and a secondary peak near 229.8 rad m^{-2}. (c) Linear (L/I, green histogram and dashed line) and circular (V/I, purple histogram and solid line) polarization fractions. (d) Intrinsic polarization position angle (PA$_0$), corrected for Faraday rotation.

respectively. The quoted uncertainties correspond to fractional model uncertainties of 12.32% for YMW16 and 14.59% for NE2025, estimated from pulsars with measured DMs at similar Galactic latitude by comparing the observed DMs with the corresponding model predictions. Using the YT2020 Galactic halo model (S. Yamasaki & T. Totani 2020), we further estimate a halo contribution of $\mathrm{DM_{MW,halo}} = 45.05^{+26.34}_{-16.62}$ pc cm^{-3}, where the uncertainty is obtained by applying the $\sim$0.2 dex (rms) fluctuation reported for the Milky Way halo DM in that model. We also estimate the Galactic Faraday rotation foreground from the Galactic Faraday rotation sky map (S. Hutschenreuter et al. 2022), obtaining $\mathrm{RM_{MW}} = -14.55 \pm 10.48$ rad m^{-2}. These values are not burst-by-burst catalog entries, but source-level line-of-sight foreground references that may be useful for interpreting the measured DMs and RMs in the catalog.

4. Data Quality and Global Properties

To validate the data quality and present an overview of the source's behavior, we show the distributions of and correlations between key parameters from the catalog. This analysis serves to characterize the dataset for future scientific work and does not attempt a detailed physical interpretation.

4.1. Parameter Distributions

Figure 1 presents the histograms of the primary measured parameters for the entire burst sample.

1. *Dispersion measure (DM; upper-left panel).* The DM distribution peaks at approximately 528.9 pc cm^{-3}, consistent with previously reported values for this source (K. Shin et al. 2026). The narrow spread of the distribution demonstrates the stability of the line-of-sight integrated electron density over the 16 month observing campaign.
2. *Rotation measure (RM; upper-right panel).* The RM distribution exhibits a complex, non-Gaussian structure. The primary peak is located near 362.2 rad m^{-2}, corresponding to the initial stable phase of the source. A secondary, smaller but visually distinct peak is present at a lower RM of approximately 229.8 rad m^{-2}. This bimodality directly reflects the significant temporal evolution of the RM (see Figure 2(a)), where the secondary peak corresponds to bursts detected during the later phase of rapid RM decline and a subsequent clustering of activity.
3. *Linear/circular polarization fraction (L/I, V/I; lower-left panel).* The linear polarization fractions are systematically high, with a 3σ lower bound of 76%, a behavior commonly seen among repeating FRBs and suggestive of a magnetically ordered emission region. The distribution of the absolute circular polarization fraction is peaked at low values, with a majority of bursts below 40%. A tail of bursts extends to higher values, suggesting diverse emission properties or propagation effects within the sample.
4. *Intrinsic polarization angle (PA$_0$; lower-right panel).* The distribution of the intrinsic polarization position angles is broad, spanning the full $-90°$ to $90°$ range with a peak approximately around $10°$. It is not uniform, but exhibits a noticeable, non-Gaussian excess. While a concentration of bursts suggests a possible preferential orientation in the emission or projection geometry during parts of the observing campaign, the broad underlying distribution indicates that this preference is not stable or exclusive. The overall pattern is inconsistent with a single, stable global magnetic field direction governing all bursts.

4.2. Parameter Correlations

Figures 2–5 explore the relationships among several key parameters to assess the overall consistency of the measurements and to identify global trends in the burst sample.

1. *RM evolution (Figure 2).* Among the parameters shown in Figure 2, RM is the only one that exhibits a pronounced long-term evolution, consistent with the

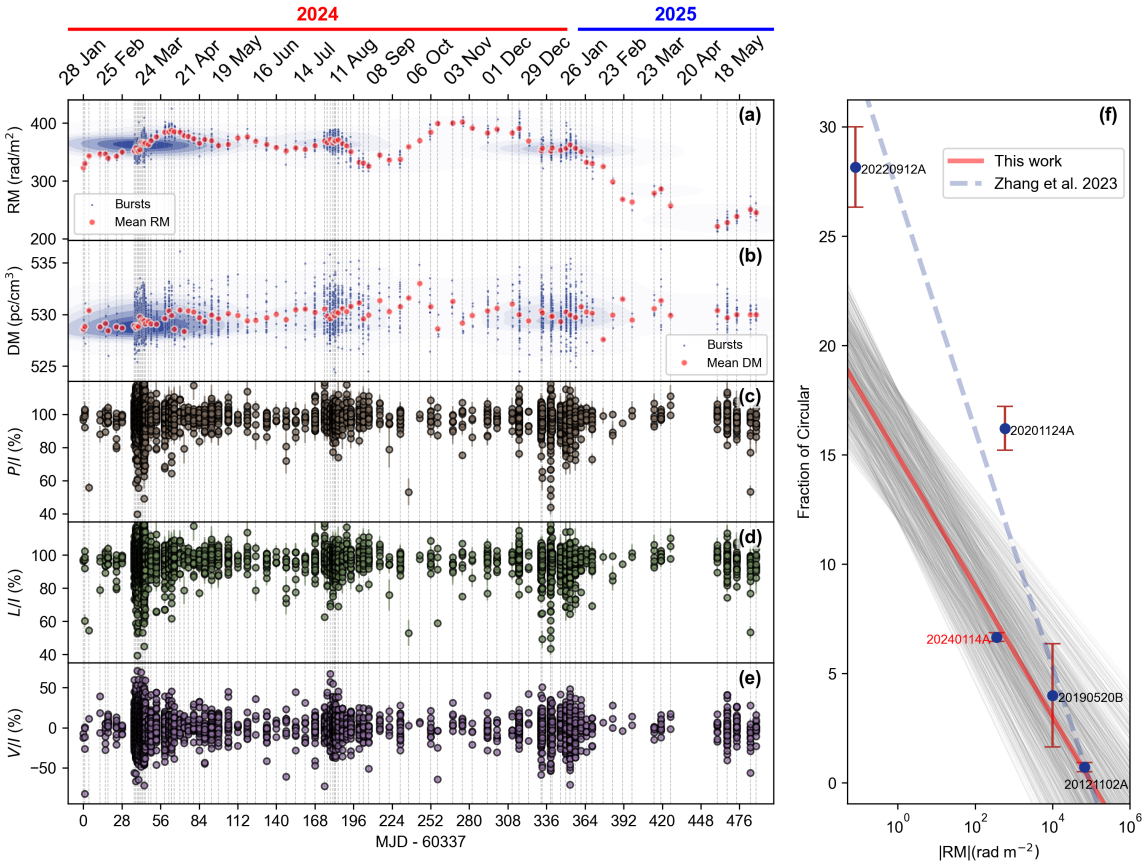


Figure 2. Temporal evolution of burst properties. Panels (a) to (e) share a common horizontal axis (topocentric MJD). (a) RM as a function of time. The blue contour is the 2D kernel density estimation (KDE) of the RM. (b) DM over time. The blue contour is the 2D KDE of the DM. (c) Total polarization fraction over time. (d) Linear polarization fraction over time. (e) Circular polarization fraction (V/I) over time. (f) The relationship between the absolute circular polarization fraction ($|V|/I$) and the absolute value of the RM (|RM|). The red solid line is the fitting for five repeating FRBs including FRB 20240114A, while the blue dashed line is the fitting for four repeating FRBs not including FRB 20240114A. Plotted in gray are the results of the allowable values from the Markov Chain Monte Carlo (MCMC) run.

trend previously noted by P. A. Uttarkar et al. (2026a). As shown in panel (a), RM as a function of topocentric arrival time displays an initial period of relative stability followed by a significant linear decay. In contrast, the corresponding time evolutions of DM, total polarization fraction (P/I), linear polarization fraction (L/I), and circular polarization fraction (V/I) shown in panels (b)–(e) do not display a similarly distinct transition, and instead remain comparatively stable or scattered without a clear monotonic trend. This RM evolution will be the focus of a more detailed analysis in a subsequent paper.

2. *Polarization fraction distribution evolution (Figure 3).* The top panel shows the observed burst number (with S/N $\geqslant$ 20) as a function of time, indicating significant variations in activity level. The middle panel quantifies the similarity between the two-dimensional (linear versus circular) polarization fraction distributions of cumulative bursts in consecutive observing sessions with different timescales using the energy distance metric (see Appendix D). A larger energy distance corresponds to lower similarity between the two distributions. The notable peaks in this metric are found to correlate with abrupt, large changes in the number of detected bursts (as seen in the top panel), rather than signifying a fundamental change in the shape of the underlying polarization distribution itself. This conclusion is visually and statistically confirmed by the semicircle diagram in the bottom panel. Across the entire $\sim$16 month span, the dense locus of points consistently resides near the high-linear-polarization, low-circular-polarization end of the theoretical limit (the semicircle boundary). The core shape and concentration of this two-dimensional distribution show no systematic evolution correlated with the drastic RM change or the variable burst rate.
3. *RM versus DM (Figure 4; left panel).* No strong correlation is observed between RM and DM across the entire dataset (Pearson correlation coefficient $r = -0.023$). This lack of correlation suggests that the RM variability is not controlled by changes in the total electron column density alone. Instead, it is consistent with a scenario in which the Faraday rotation is dominated by variations in the line-of-sight magnetic field component, including possible changes in its strength or orientation, within a complex magneto-ionic environment.
4. *RM versus PA_0 (Figure 4; right panel).* Similar to DM, the intrinsic polarization position angle (PA_0) is also separable into two groups chronologically and exhibits no strong correlation (Pearson correlation coefficient $r = -0.049$). The distribution in PA_0 is broader for a given RM, resulting in two vertical columns rather than

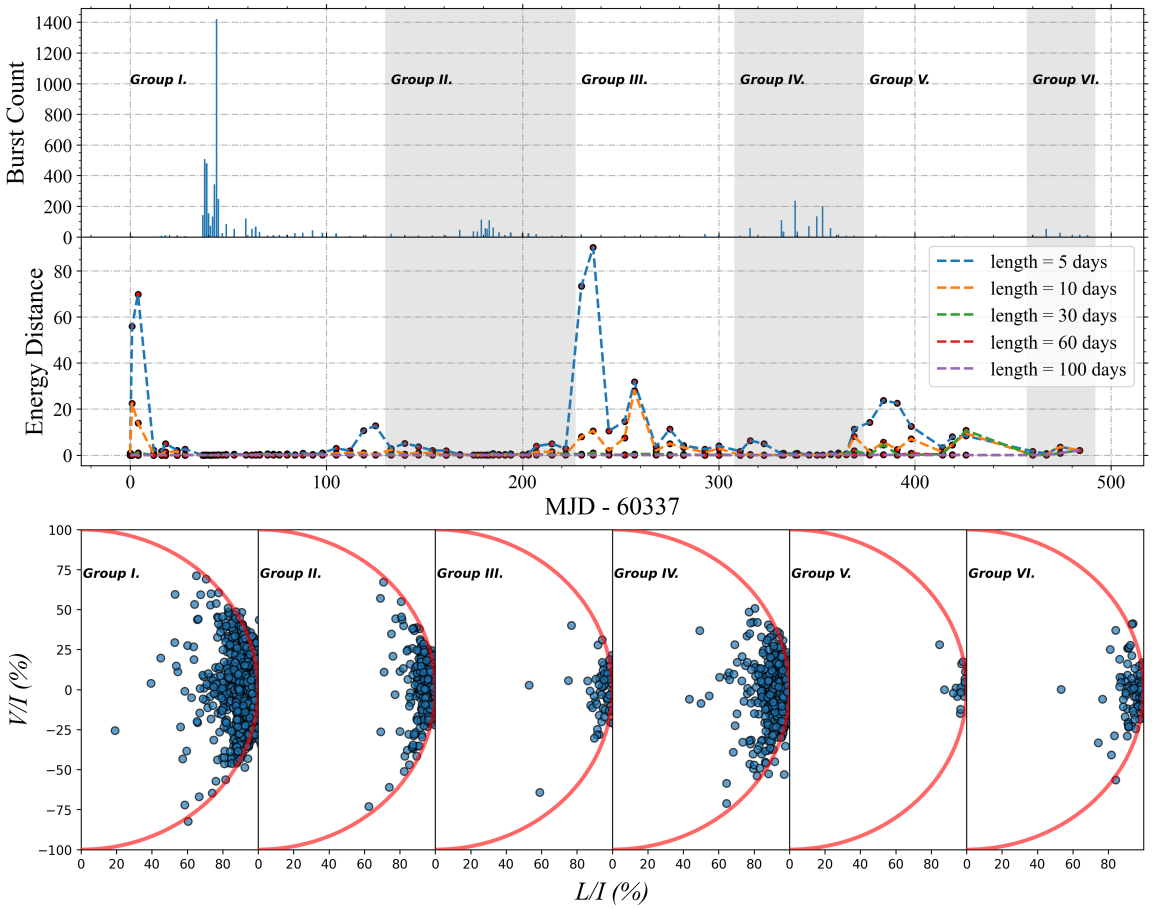


Figure 3. Temporal evolution of linear and circular polarization fraction distributions. (Top) Histogram of the number of bursts with S/N $\geqslant$ 20 per observing session. The timeline is divided into six alternating shaded/unshaded sessions (I–VI) based on burst activity. (Middle) Energy distance (a statistical measure of similarity between distributions) calculated between the polarization fraction distributions of cumulative bursts in consecutive observing sessions with different timescale cumulative windows. Some peaks in energy distance correspond to sessions with a sudden, large change in the number of data points (bursts) rather than a genuine shift in the underlying distribution shape. (Bottom) Temporal evolution of the polarization fraction distributions visualized for sessions I–VI using a semicircle diagram.

compact clusters. This indicates that while the RM (probing the line-of-sight magnetic field) changed systematically, the intrinsic PA (related to the emitting region magnetic geometry) retained a wide range of orientations throughout the evolution.

5. *Polarization fraction versus S/N (Figure 5).* The linear and circular polarization fractions are plotted against the burst S/N (left and middle panel). As expected, the measurement uncertainty increases at low S/N. The absence of any spurious trends at high S/N confirms the robustness of our polarization calibration and debiasing procedures (see Appendix B). The right panel shows the relationship between the linear (L/I) and circular (V/I) polarization fractions. A theoretical semicircle with a radius of 100%, centered on the origin and extending in the positive L/I direction, is overlaid. This curve represents the physical limit for fully polarized emission. The points are color coded by the burst S/N, and number-density contours are added to illustrate the distribution of the large dataset. Two key features are evident: (1) The vast majority of data points, especially those with high number density, cluster near the intersection of the semicircle and the L/I axis (i.e., high linear and low circular polarization). (2) Points lying outside the theoretical semicircle are predominantly those with low S/N. This is fully consistent with expectations, as measurement noise can spuriously push low-S/N points beyond the physical boundary, further validating our error estimation and the overall quality of the polarimetric measurements.

In addition to the above parameters, we also calculated the proportion of bursts exhibiting significant circular polarization (degree of circular polarization; $|V|/I \geqslant 10\%$) in our sample. For FRB 20240114A, 1157 out of 17,356 detected bursts met this criterion, yielding a proportion of 6.67% (see Figure 2(f)). This measurement was examined within the context of the tentative anticorrelation between the significant circular polarization fraction and the absolute value of the source's rotation measure (|RM|) suggested by Y.-K. Zhang et al. (2023). A power-law fit to our updated sample yields an index of -2.98 ± 0.80. With this fit, the associated uncertainty envelope encompasses the data points for FRB 20190520B and FRB 20121102A (Y. Feng et al. 2022a; Y.-K. Zhang et al. 2023), while those for FRB 20220912A and FRB 20201124A (Y.-K. Zhang et al. 2023) lie significantly outside of it. Should an underlying physical correlation exist, the fact that only a subset of sources aligns with the best-fit trend may point to intrinsic diversity within the repeating FRB population.

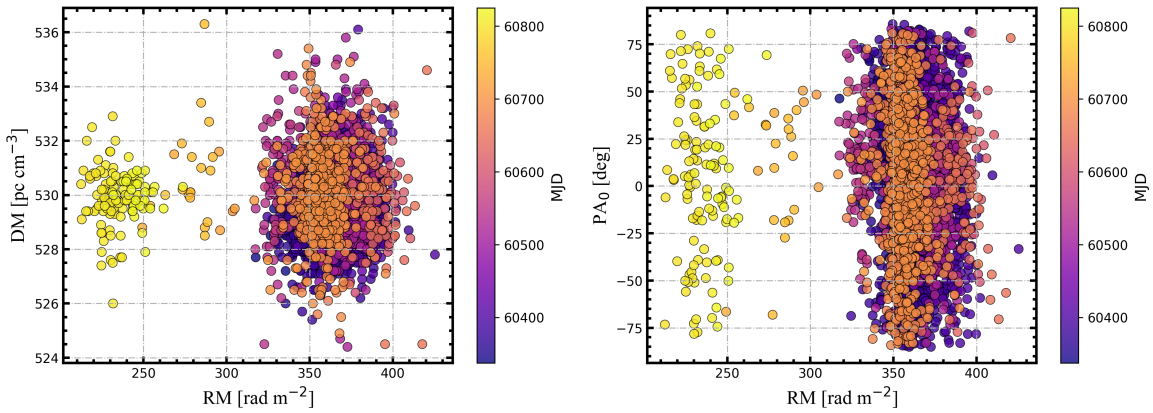


Figure 4. Rotation measure plotted versus dispersion measure and polarization position angle. (Left) RM versus DM, with points color coded by topocentric MJD. (Right) RM versus intrinsic polarization position angle (PA_0), similarly color coded.

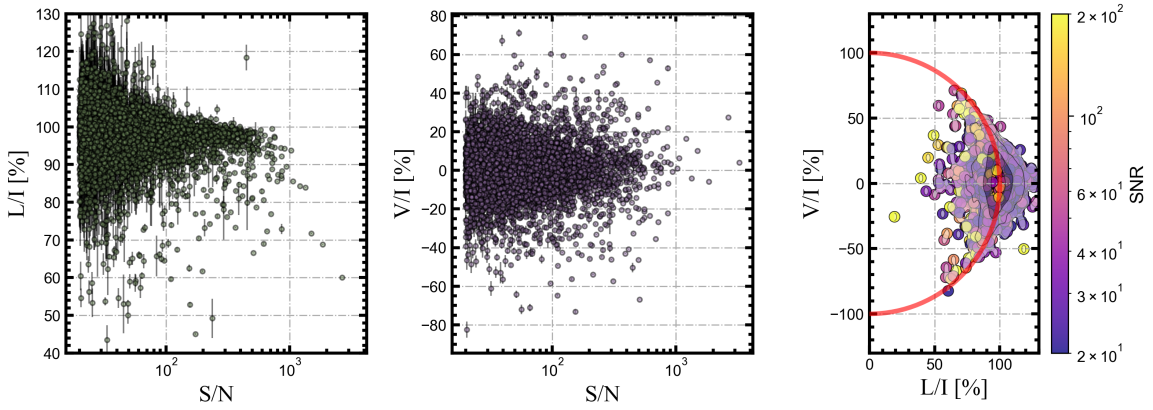


Figure 5. Relationships involving polarization fractions and S/N. (a) Linear polarization fraction (L/I) versus S/N. (b) Circular polarization fraction (V/I) versus S/N. (c) Relationship between linear and circular polarization fractions. Points are color coded by S/N, and number-density contours (gray lines) illustrate the distribution of the large dataset. The solid red semicircle represents the theoretical physical limit for 100% polarized emission.

Sources following the relation might originate in environments where the observed circular polarization is dominantly shaped by the same large-scale, ordered magneto-ionic medium responsible for the Faraday rotation (C.-H. Niu et al. 2022; R. Anna-Thomas et al. 2023). In contrast, the significant deviation of other sources could imply that their polarization properties are governed by additional or distinct physical processes. For instance, complex local Faraday screens, burst emission geometries that favor strong intrinsic circular polarization, or magnetospheric propagation effects could decouple the observed circular polarization from the bulk RM in these objects (G. H. Hilmarsson et al. 2021; H. Xu et al. 2022; R. Mckinven et al. 2023b). This dichotomy underscores that any universal relationship between circular polarization and RM is likely nuanced and modulated by source-specific conditions. It should be noted that this alignment with the trend for FRB 20240114A does not necessarily imply that the generation mechanism of circular polarization is identical to that of sources such as FRB 20121102A. Therefore, the circular polarization of FRB 20240114A may still be attributed primarily to the intrinsic emission mechanism itself, rather than being dominated by propagation effects.

In summary, the power-law fit reveals a shallower index for the $|V|/I$–$|\mathrm{RM}|$ relation, which is consistent with only a subset of repeating FRBs. This suggests that any such correlation is not universal but is likely modulated by source-specific local environments, as evidenced by the diverse RM behaviors predominantly attributed to proximate magneto-ionic screens. The dichotomy between sources that follow and those that deviate from the trend points to intrinsic diversity in either the emission mechanism or the magneto-ionic properties of the immediate vicinities of repeaters (Y.-P. Yang et al. 2023; P. A. Uttarkar et al. 2024). Continued observations of FRB 20240114A, together with comparisons across a larger sample of repeating FRB sources, will be crucial for disentangling these physical effects.

Having characterized the parameter distributions and correlations for FRB 20240114A, we next examine the frequency-dependent depolarization to explore the burst's magneto-ionic environment. A random magnetic field component within the Faraday rotating screen would cause frequency-dependent depolarization, characterized by a decrease in the observed linear polarization fraction (L/I) toward lower frequencies. In the classical B. J. Burn (1966) framework for depolarization by Faraday dispersion, the fractional reduction in linear polarization can be written as

$$f_{\mathrm{RM\ scattering}} \equiv 1 - \exp(-2\lambda^4\sigma_{\mathrm{RM}}^2), \quad (1)$$

where $f_{\mathrm{RM\ scattering}}$ is the fractional reduction in the linear polarization amplitude, σ_{RM} is the standard deviation of RM,

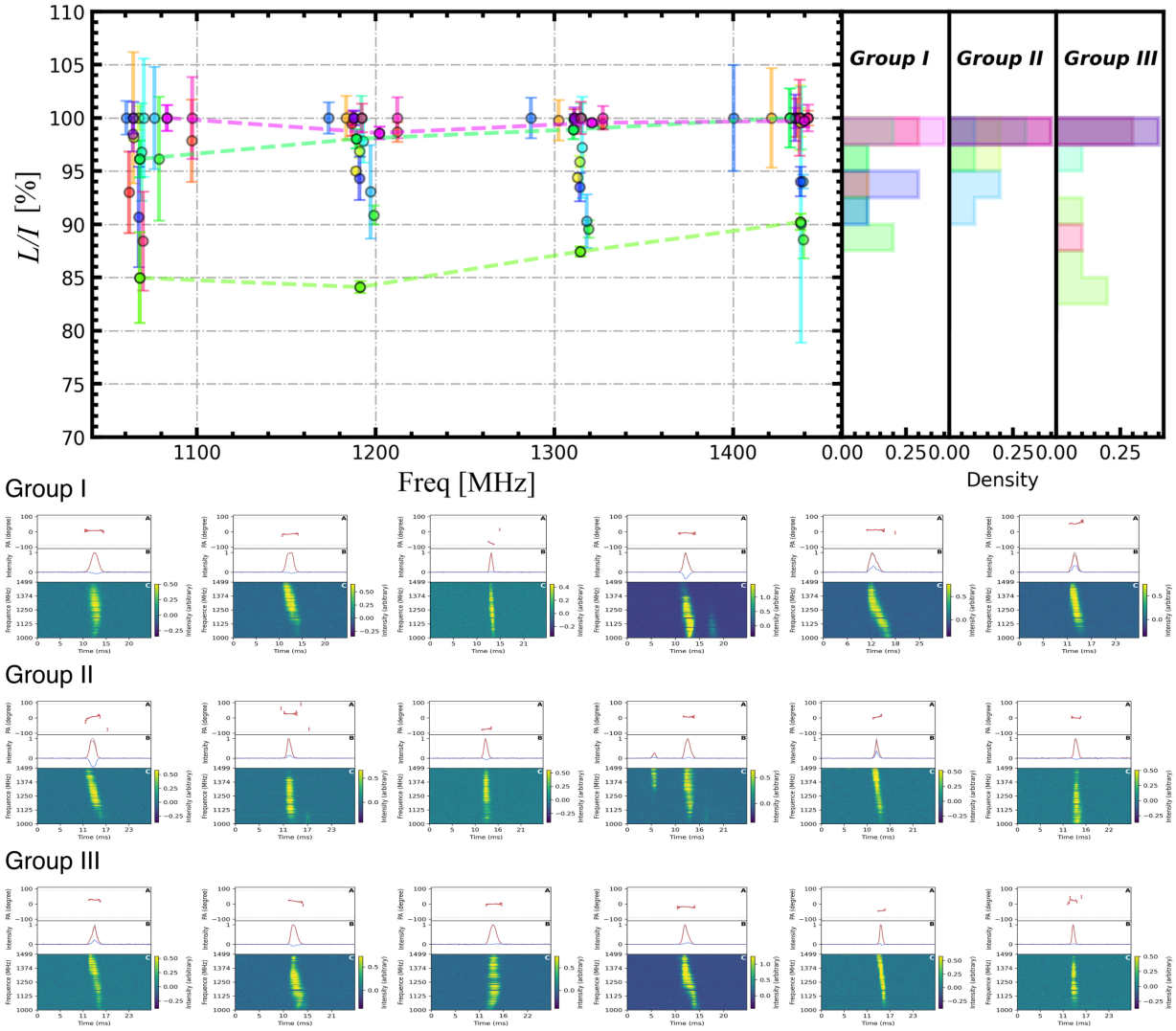


Figure 6. Test for frequency-dependent depolarization ($\sigma_{\rm RM}$). For 18 bright, broadband bursts with high S/N, we subdivided each burst's bandwidth into segments, independently measured the RM and linear polarization fraction (L/I) in each segment, and plotted L/I against the center frequency of the segment. Points are color coded by burst ID. To illustrate the frequency dependence of the L/I, three bursts were randomly selected, and their points were plotted as line plots. To avoid overlap, the 18 bursts are randomly divided into three groups for display. The 18 plots in the bottom panel show the dynamic spectrum and polarization profile for these bursts.

and λ is the wavelength. This formalism has since been applied to FRBs by Y. Feng et al. (2022b), P. A. Uttarkar et al. (2026b), and A. Pandhi et al. (2026). To test for this effect, we selected 18 bright bursts with high S/N and broad BW. The dynamic spectra and polarization profiles of these 18 bursts are shown in Figure 6. Each burst's band was subdivided into several frequency sub-bands. We independently performed RM synthesis and measured L/I within each sub-band. As shown in Figure 6, the derived L/I values for all sub-bands across all selected bursts cluster near 100%, with no systematic trend as a function of frequency. To better illustrate whether the L/I varies significantly with frequency, we plotted the L/I distribution of slices for each burst (left panel of Figure 6). To avoid overlap, the bursts were randomly divided into three groups. If the L/I distribution of a burst exhibits significant broadening, it would indicate a pronounced frequency evolution of the L/I, whereas a concentrated distribution implies that the L/I is nearly independent of frequency. The results show that the L/I distributions of all 18 bursts are relatively concentrated, indicating that the L/I remains nearly constant across frequency. This absence of significant depolarization allows us to place an upper limit on any random magnetic field component (often quantified as $\sigma_{\rm RM}$) within the main Faraday screen. Based on our Bayesian analysis of 18 bursts, we derive a 95% upper limit of $\sigma_{\rm RM} < 0.51\,\mathrm{rad\ m^{-2}}$. This suggests that the main Faraday screen is largely ordered and exhibits minimal internal Faraday dispersion, at least for the selected bursts analyzed here. A broader population-level test based on burst central frequency, BW, and L/I would be valuable, but is not yet sufficiently robust for the present dataset because our current CDF-based BW measurements do not always yield reliable central frequency estimates, particularly for bursts truncated by the band edges. In addition, for multicomponent bursts, differences in L/I among distinct temporal or spectral components may contaminate a depolarization search by introducing apparent

frequency-dependent behavior that does not arise from a single, uniform Faraday screen.

We additionally searched for signatures of Faraday conversion in bursts with sufficient S/N and frequency coverage. Specifically, we examined whether the circular polarization fraction exhibits any systematic frequency- or wavelength-dependent evolution within individual bursts. We do not find any clear or definitive evidence for such behavior in the present sample. This is also consistent with the result of P. A. Uttarkar et al. (2026a).

5. Discussion

5.1. The Origin of RM Evolution

Our session-based analysis (Figure 7) starkly contrasts the temporal behaviors of DM and RM. The DM remains stable across all six activity-defined sessions, with its distribution peak and width showing negligible changes (Figure 7(e)). This indicates that no strong secular DM evolution is detected across the six activity-defined sessions. To quantify the additional burst-to-burst DM scatter beyond the formal fitting uncertainties, we compared the burst-level DMs with the corresponding daily average reference DM values and wrote the observed daily scatter as $\sigma^2_{\rm obs,daily} = \sigma^2_{\rm measure} + \sigma^2_{\rm sys} + \sigma^2_{\rm int}$, where $\sigma_{\rm measure}$ is the formal measurement contribution, $\sigma_{\rm sys}$ represents the morphology-related excess variance, and $\sigma_{\rm int}$ denotes any intrinsic day-scale DM variation. For our sample, we obtain $\sigma_{\rm obs,daily} = 1.10\,{\rm pc\,cm^{-3}}$ and $\sigma_{\rm measure} = 0.84\,{\rm pc\,cm^{-3}}$, implying $(\sigma^2_{\rm sys} + \sigma^2_{\rm int})^{1/2} \approx 0.70\,{\rm pc\,cm^{-3}}$. Under the practical assumption that $\sigma_{\rm int} = 0$, this yields an upper limit of $\sigma_{\rm sys} \lesssim 0.70\,{\rm pc\,cm^{-3}}$. We therefore interpret the absence of an obvious long-term DM trend as a nondetection above the burst-level variance floor, rather than as evidence for perfectly constant DM. This interpretation is also supported by the recent FAST study of Y. Feng et al. (2026), who argued that part of the apparent burst-to-burst DM scatter in repeating FRBs can be morphology-induced ("pseudo DM") rather than reflecting true propagation changes. Our result for FRB 20240114A is qualitatively consistent with this picture. In dramatic contrast, the RM undergoes a highly significant, monotonic decay of approximately 200 rad m^{-2}. The shift in the RM distribution peak between sessions is visually clear (Figure 7(e)).

To quantify the significance of this decline, we performed a Monte Carlo test using the burst-level RM measurements from sessions I–IV as the null hypothesis of a stable RM distribution. Specifically, we combined all RM values from these four sessions and used their sample mean and standard deviation to define the parent distribution. We then generated 10,000 mock samples, each containing the same number of bursts as observed in sessions V–VI, by drawing random values from this null distribution. For each mock sample, we calculated its mean RM and compared the resulting distribution of simulated means with the observed mean RM of sessions V–VI. The observed value lies far below the simulated distribution, and none of the 10,000 realizations reproduces such a low mean, implying $p < 10^{-4}$ under the null hypothesis of no RM evolution.

The evolution of the line-of-sight magnetic field component $\langle B_\parallel \rangle$ can be quantitatively estimated from the changes in RM and DM, which is given by $\langle B_\parallel \rangle \simeq 1.2 \times \Delta{\rm RM}/\Delta{\rm DM}\,\mu{\rm G}$, where ΔRM and ΔDM are the differences in RM and DM between different sessions. Applying this to the significant RM decay observed between activity sessions, we find that the nominal values of $\langle B_\parallel \rangle$ vary in a manner qualitatively consistent with the RM evolution (Figure 7(d)). However, the uncertainties are large, and the current data do not provide statistically significant evidence for a departure from a constant temporal evolution of $\langle B_\parallel \rangle$. The uncertainties of $\langle B_\parallel \rangle$ are derived from error propagation of the measurement errors in RM and DM. The stable standard deviation of DM over time (Figure 7(a)) argues against the injection of new, clumpy plasma, supporting the interpretation that the changing RM and $\langle B_\parallel \rangle$ stem from the evolution of an existing magneto-ionic environment.

This inferred local line-of-sight magnetic field can also be compared with similar estimates discussed for other repeating FRBs. For FRB 20240114A, our session-based estimates span from values consistent with zero at early times to tens and up to $\sim 10^2\,\mu$G at later epochs, with nominal values ranging from about -168 to $+54\,\mu$G (i.e., $\sim$0.05–0.17 mG in magnitude). This places FRB 20240114A below the more strongly magnetized mG-class environments inferred for FRB 20121102A (D. Michilli et al. 2018), FRB 20190520B (R. Anna-Thomas et al. 2023), FRB 20190417A (A. M. Moroianu et al. 2026), and FRB 20220529A (A. Pandhi et al. 2026), and also somewhat below FRB 20240619D (O. S. Ould-Boukattine et al. 2026). In this sense, FRB 20240114A appears less extreme than highly magnetized systems, while still indicating a dynamically evolving magneto-ionic environment. More broadly, it is comparable to the class of repeaters for which RM and DM evolution imply a local environment that is clearly magnetized but not as extreme as the most strongly Faraday-active sources.

The coherent, large-scale decay in both RM and the inferred $\langle B_\parallel \rangle$ points to a global evolution of the magneto-ionic environment surrounding the FRB source. This could be due to the expansion of a magnetized shell (e.g., an SNR or a pulsar wind nebula; D. Michilli et al. 2018), the traversal of the source through a gradient in a large-scale magnetic field, or the secular evolution of a magnetized stellar wind from a binary companion (H. Xu et al. 2022).

A useful phenomenological comparison is FRB 20180916B, whose RM evolution also exhibits an initially relatively stable phase followed by a more secular change (R. Mckinven et al. 2023b). In that sense, FRB 20240114A does not appear to be an isolated case, but may belong to a subset of repeaters whose magneto-ionic environments evolve smoothly over month-to-year timescales rather than through purely stochastic fluctuations. At the same time, the detailed amplitudes, durations, and possible reversals of the RM evolution differ between sources, indicating diversity in the underlying environments and evolutionary drivers.

5.2. Complex and Variable Emission Geometry

Recent systematic studies of large samples of repeating FRBs observed with FAST have revealed that while some bursts exhibit PA swings consistent with the rotating vector model (RVM), the fitted geometric parameters and effective spin periods are highly inconsistent across bursts. This suggests that the magnetosphere of the FRB central engine is constantly distorted by the FRB emitter, leading to a dynamically evolving magnetic configuration rather than a stable dipole structure (X. Liu et al. 2025).

The polarization position angle evolution of FRB 20240114A also exhibits this dynamic characteristic. For each

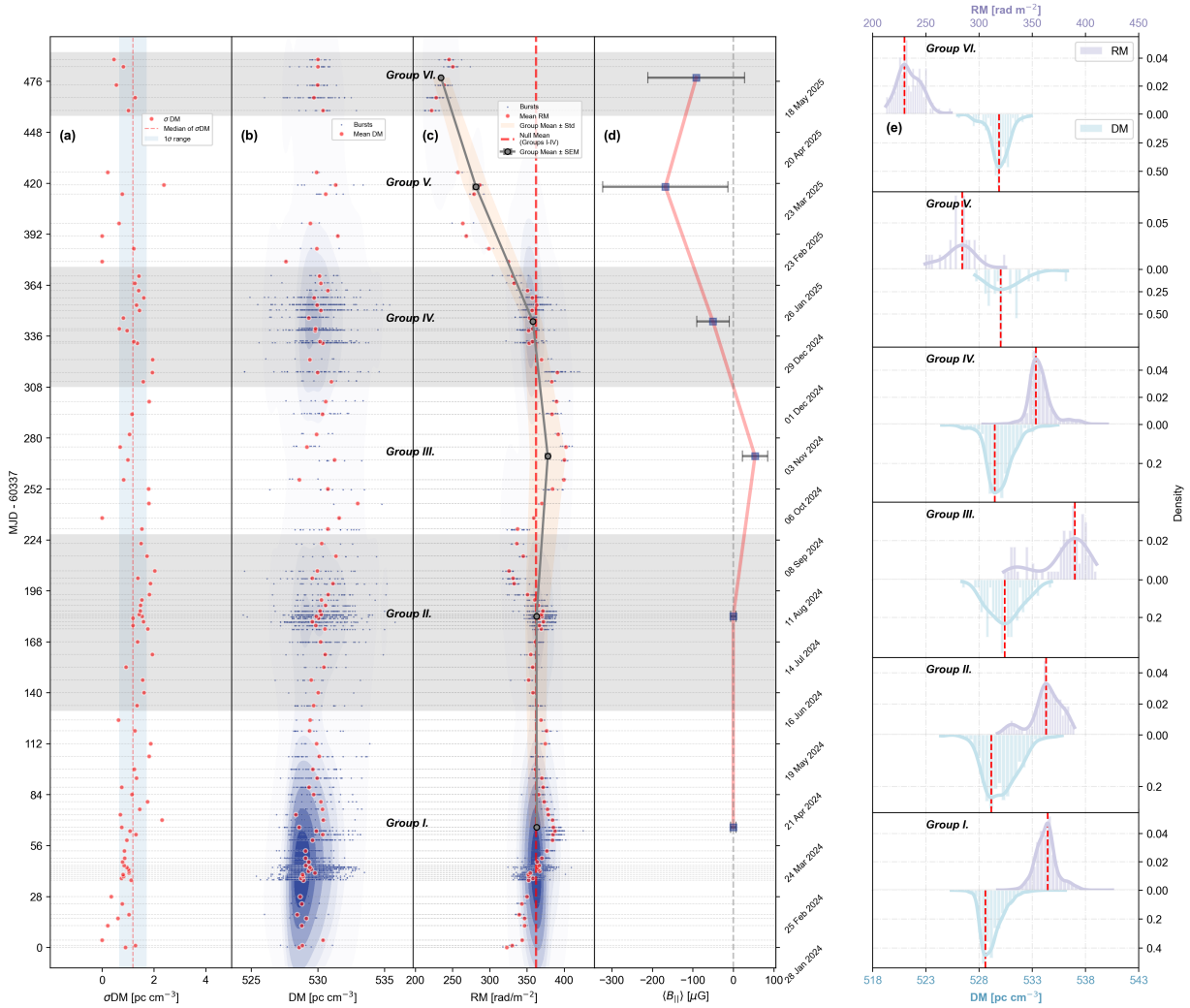


Figure 7. Temporal evolution of DM, RM, and $\langle B_{\parallel} \rangle$. Panel (a): The temporal evolution of $\sigma_{\rm DM}$, where $\sigma_{\rm DM}$ denotes the standard deviation of the burst DM measurements within each observing interval. The red dashed line represents the median, and the light blue shaded area indicates the 1σ range. Panels (b) and (c): The temporal evolution of DM and RM is displayed with MJD on the vertical axis. The blue contours represent the two-dimensional KDE of the data points. The timeline is divided into six alternating shaded/unshaded sessions (I–VI) based on burst activity. In the RM panel, gray solid lines with error bars show the standard error of the mean (SEM) for bursts within contiguous time bins, and the orange band indicates the standard deviation. The red dashed line marks the mean RM under the null hypothesis of no magnetic field evolution. Panel (d): the evolution of $\langle B_{\parallel} \rangle$ for six sessions. Panel (e): The corresponding distributions of RM (top subpanel) and DM (bottom subpanel) for each of the six sessions (I–VI, from bottom to top). The red dashed lines indicate the peak of each distribution.

burst, we first determine its RM and derotate the Stokes Q and U data accordingly. We then construct a time-resolved PA profile from the frequency-summed derotated Stokes parameters. The uncertainty of each PA sample, denoted as PAE, is estimated by propagating the off-pulse noise in Q and U; only on-pulse samples with PAE $\leqslant 10^{\circ}$ are retained. We define $\rm PA_0$ as the time average of the retained derotated PA samples for each burst. Unlike FRB 20180916B, which shows remarkably stable burst-to-burst PAs indicative of a highly stable magnetic field geometry at the emission site (S. Bethapudi et al. 2025), FRB 20240114A exhibits large burst-to-burst PA variation (Figure 8). Using the reduced-χ^2 of a constant-PA fit to the derotated time-resolved PA profiles, we find that 67.2% of bursts satisfy $\chi^2_{\nu} < 5$. However, $\chi^2_{\nu} \geqslant 5$ does not necessarily imply a prominent PA swing; if we additionally require the difference between the maximum and minimum PA within a burst to exceed 40°, the fraction of bursts with clear intraburst PA swings is 17.6%. For bursts with variable PA profiles, $\rm PA_0$ should therefore be regarded as a representative value rather than a complete description of the full intraburst PA evolution. The broad distribution of $\rm PA_0$, even for bursts with stable intraburst PA profiles (blue histogram in Figure 8), and the significant scatter of the session-averaged $\rm PA_0$ (red error bars in Figure 8, left) suggest that the bursts originate from a spatially complex or temporally fast-evolving magnetospheric environment. The lack of a stable, globally preferred PA challenges models where emission is strictly confined to a fixed magnetic pole. The combination of a systematically evolving RM (probing the large-scale, intervening screen) and a highly variable PA (probing the immediate emission geometry) suggests that both the large-scale environment and the small-scale emission region are dynamic, albeit likely on different timescales.

Interestingly, independent observations of FRB 20240114A with the Parkes ultrawideband low (UWL) receiver have revealed a multipeak distribution in the polarization position angle, with excesses near $-17^{\circ}.39$ and $64^{\circ}.8$ (P. A. Uttarkar et al. 2026a). This contrasts with the PA distribution observed in our FAST data,

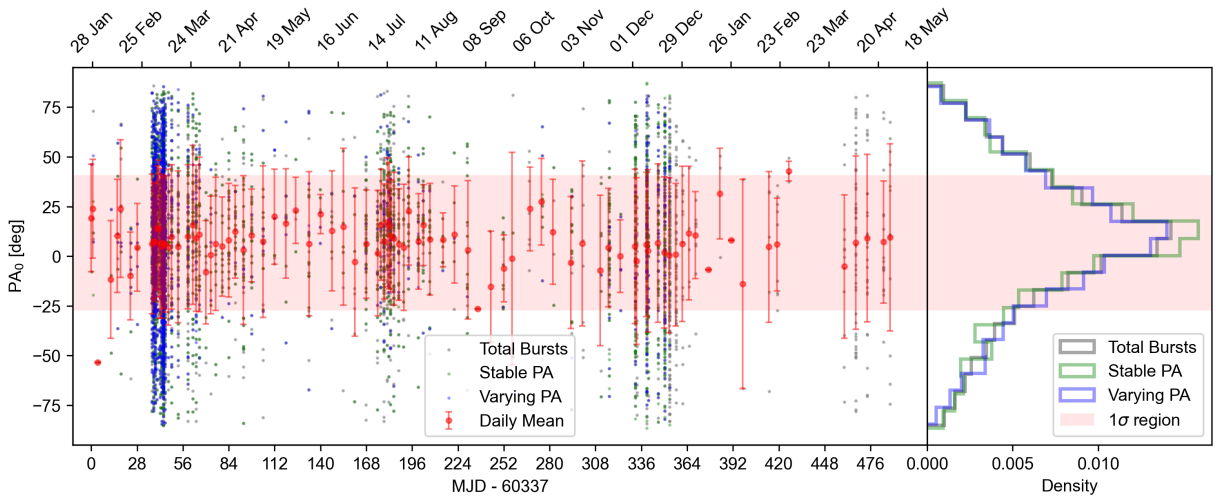


Figure 8. Temporal evolution and distribution of the intrinsic polarization position angle (PA_0). (Left) PA_0 as a function of time. Bursts are color coded based on the reduced chi-square (χ^2_ν) of a constant-PA fit to their time-resolved, frequency-averaged PA measurements: green points indicate bursts with stable PA profiles ($\chi^2_\nu <$ 5), while blue points indicate bursts with variable PA profiles ($\chi^2_\nu \geqslant 5$; A. Pandhi et al. 2024). The red points with error bars represent the mean PA_0 and its standard deviation for each observing session. (Right) Histograms of the PA_0 distribution. The gray histogram includes all bursts, with the shaded region marking the $\pm 1\sigma$ range. The green histogram includes only bursts with stable PA profiles (green points from the left panel) while the blue histogram includes bursts with variable PA profiles (blue points from the left panel). The red-shaded 1σ region highlights the significant burst-to-burst PA variation present in the full sample.

suggesting that the apparent PA distribution may depend on the observed frequency band or the specific activity epoch. Such frequency-dependent PA behavior would be expected in a dynamically evolving magnetosphere, where different emission heights or regions could be probed at different frequencies. However, the effect appears to be relatively weak, as both datasets consistently point to a highly variable emission geometry without a single preferred direction.

5.3. Comparison with Other Repeaters and the Origin of Periodicity

The possible quasiperiodic modulation of burst activity in FRB 20240114A reported by P. A. Uttarkar et al. (2026a) introduces an additional layer of complexity to the understanding of this source. Using Murriyang observations, they proposed a timescale of approximately 70 days and interpreted it as evidence for plasma lensing due to extreme scattering events. D. Zhou et al. (2026) have also identified periodicities in FAST observations of this source, with periods of 143.40 ± 7.19 days (5.2σ significance) and 73.60 ± 2.45 days (3.3σ significance). Notably, periodic phenomena are not unique to FRB 20240114A. Several well-studied repeating FRBs have been reported to exhibit periodicities in either their burst activity or environmental properties, including FRB 20180916B, which shows a 16.35 day activity period (CHIME/FRB Collaboration et al. 2020). In this context, any potential activity periodicity in FRB 20240114A would place it among a small but growing group of repeaters with long-term activity modulation. The diversity of reported activity-modulation timescales among repeaters suggests that multiple physical mechanisms may be at play. The interpretation of any potential periodicity in FRB 20240114A thus remains an open question, necessitating further monitoring and multiwavelength observations to distinguish between intrinsic and environmental origins.

6. Summary and Data Access

In this paper, we present a large-scale polarization catalog for the repeating FRB 20240114A, resulting from an extensive monitoring campaign with the FAST telescope between 2024 January 28 and 2025 May 30. The core of this work is the detection and parameterization of 6131 bursts. We have detailed the comprehensive data processing pipeline, from initial data acquisition and preprocessing to sophisticated polarization calibration and RM synthesis. The key deliverables of this pipeline are precise measurements for each burst, including the topocentric arrival time (MJD), DM, pulse width, BW, RM, and the degrees of linear and circular polarization.

The global analysis of this catalog reveals several key characteristics of the source:

1. *Dynamic rotation measure*. The RM exhibits a remarkable two-phase temporal evolution: an initial period of relative stability around a mean value, followed by a rapid, near-linear decay of approximately 200 rad m^{-2} over about 200 days. This evolution manifests as a bimodal distribution in the RM histogram. The joint RM–DM temporal analysis indicates that the RM variation is dominated by changes in the line-of-sight magnetic field strength rather than electron column density, implying a dynamically evolving magnetized environment in the immediate vicinity of the source.
2. *Stable dispersion measure*. In contrast to the RM, the DM remains remarkably stable throughout the entire observing campaign, indicating a constant integrated electron density along the line of sight.
3. *High degree of polarization.* The linear polarization fraction is generally high, while the circular polarization is typically low. The relationship between linear and circular polarization for the vast majority of bursts adheres to the theoretical physical limit, with outliers primarily attributed to low-S/N measurements. The intrinsic polarization position angle distribution is broad

and centered near 10° with a non-Gaussian excess, but shows no stable, singular preferred orientation over time.

4. *Stable polarization fraction distributions*. Despite the dramatic evolution in RM, the combined two-dimensional distribution of linear versus circular polarization fractions remains statistically stable across the entire observing period. This suggests that the underlying emission mechanism and the net ordered magnetic field geometry in the immediate emission region are largely invariant.
5. *Absence of frequency-dependent depolarization*. Analysis of bright, broadband bursts shows no systematic decrease in linear polarization fraction with frequency, arguing against significant random magnetic fields ($\sigma_{\rm RM}$) within the main Faraday rotating screen.
6. *Absence of Faraday conversion*. No significant Faraday conversion is detected at any epoch. This nondetection indicates that the polarization data probe only the line-of-sight magnetic field component. The perpendicular component remains unconstrained. Future ultrawideband and higher-sensitivity observations may detect conversion. This would enable joint tracking of the perpendicular and parallel magnetic field components, and allow reconstruction of the time-varying three-dimensional magnetic field in the source vicinity.

The global distributions and correlations of these parameters, presented in Section 4, attest to the high quality and internal consistency of the catalog. They reveal a source with a stable DM but a highly dynamic RM, complex polarization behavior, and no simple correlation between DM and RM. These features underscore the value of this uniform, high-sensitivity dataset for statistical and temporal evolution studies.

The complete catalog is publicly available to the scientific community to maximize its utility. The catalog, in CSV format, can be accessed through the following permanent repositories at doi:10.57760/sciencedb.Fastro.00040. The original observational data are available from the FAST archive at https://fast.bao.ac.cn/.

The catalog is also available as a machine-readable table online. We encourage the community to use this catalog for further investigations.

Acknowledgments

We thank the staff of the FAST telescope for their support during the observations. FAST is a Chinese national mega-science facility, built and operated by the National Astronomical Observatories, Chinese Academy of Sciences. This work made use of the data from the FAST FRB Key Science Project and the data of the CHIME/FRB VOEvent Service, BlinkVerse, and TransientVerse.

This study is supported by the National Natural Science Foundation of China (NSFC) Program Nos. 12588202, 11690024, 11725313, 11988101, 12041303, 12203045, 12233002, 12303042, 12403100, 12421003, 12447115, 12522305, 12541304, 12373040, U1731238, U2031117, W2442001; the CAS International Partnership Program No. 114-A11KYSB20160008; the CAS Strategic Priority Research Program No. XDB23000000; the National Key R&D Program of China Nos. 2021YFA0718500, 2023YFE0110500, QN2023061004L, 2024YFA1611703, 2024YFA1611700; the National SKA Program of China No. 2022SKA0130104; the China Postdoctoral Science Foundation (CPSF) under grant Nos. GZB20240308, GZB20250737, 2025T180875; and the Fundamental Research Funds for the Central Universities. P.W. acknowledges support from the CAS Youth Interdisciplinary Team, the Youth Innovation Promotion Association CAS (id. 2021055), and the Cultivation Project for FAST Scientific Payoff and Research Achievement of CAMS-CAS. D.L. is a New Cornerstone investigator. W.-W.Z. is supported by the CAS Project for Young Scientists in Basic Research, YSBR-063. Y.-F.H. is supported by the Xinjiang Tianchi Program. Y.F. is supported by the Leading Innovation and Entrepreneurship Team of Zhejiang Province of China grant No. 2023R01008. W.-Y. W. acknowledges support from the NSFC (No.12261141690 and No.12403058), and the Strategic Priority Research Program of the CAS (No. XDB0550300). J.-R.N. is supported by the National Natural Science Foundation of China (NSFC, No. 12503055) and the Postdoctoral Fellowship Program of CPSF under grant No. GZB20250737. R.-S.Z. is supported by the National Natural Science Foundation of China (grant No. 12563008), Science and Technology Foundation of Guizhou Provincial Department of Education (No. KY(2023)059), and Liupanshui Science and Technology Development Project (No. 52020-2024-PT-01). Q.W. is supported by the National Natural Science Foundation of China (grant Nos. 12447115 and 12503050) and the China Postdoctoral Science Foundation (CPSF) under grant No. GZB20240308, 2025T180875, and 2025M773199. E.G. is supported by the Doctor Foundation of Qingdao Binhai University (No. BJZA2025025).

Facility: FAST:500m

Software: astropy (Astropy Collaboration et al. 2013), SciPy (P. Virtanen et al. 2020), DM-power (H.-H. Lin et al. 2022), PRESTO (S. M. Ransom 2001), DRAFTS (Y.-K. Zhang et al. 2025), PSRCHIVE (A. W. Hotan et al. 2004), ionFR (C. Sotomayor-Beltran et al. 2013).

Author Contributions

All authors discussed the contents and formed the final version of the paper.

Appendix A
Polarization Calibration

The polarization of the detected bursts was calibrated by correcting for differential gains and phases, using separate measurements of a noise diode injected at an angle of 45° from the linear receiver. This was done with the software package PSRCHIVE (A. W. Hotan et al. 2004). The circular polarization of most bursts is consistent with noise, being less than a few percent of the total intensity, in agreement with the findings of D. Michilli et al. (2018).

Saturation occurs in the FAST receiver when radio flux densities reach levels between hundreds of Jansky and mega-Jansky. To identify potential saturation events and mitigate their impact on polarization analysis, each burst's four polarization components (XX, YY, X^*Y, and Y^*X) were systematically examined. Here the quoted thresholds refer to the raw stored intensity values in the FAST FITS files rather than calibrated physical units. Saturation manifests differently across components: XX and YY saturate when intensities exceed 255 (wrapping to 0), while X^*Y and Y^*X saturate when absolute intensities surpass 127 (also wrapping to 0). For every burst, the dynamic spectra of all four polarization components were inspected. Critical-value data points (corresponding to the 255 and 127 thresholds) were flagged on the total intensity (I)

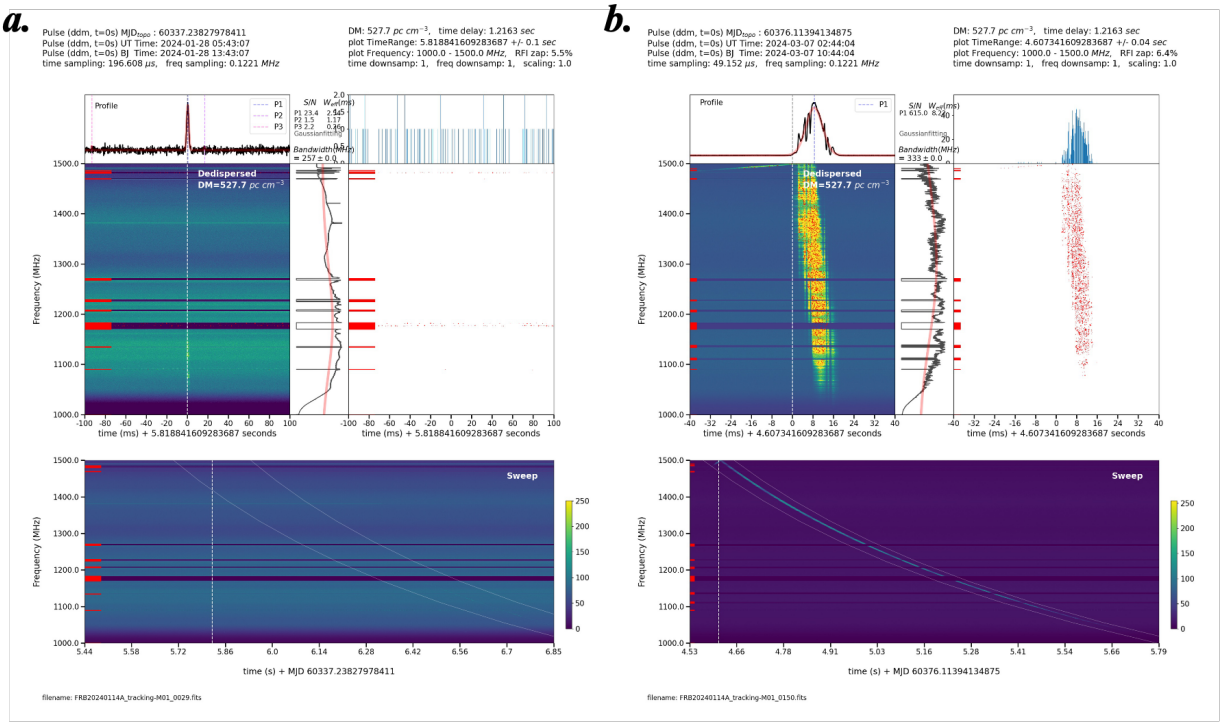


Figure 9. Examples of dynamic spectra (waterfall plots) illustrating the identification of anomalous samples. In both cases, radio-frequency interference (RFI) and samples affected by signal saturation are marked in red. (a) A burst without saturation. The red points are predominantly confined to specific, persistent RFI frequency channels. Consequently, the time profile of these flagged samples shows a relatively uniform distribution, reflecting the continuous nature of the RFI. (b) A burst with saturation. The red points are concentrated within the bright, central region of the burst itself, indicating that the high signal strength has driven the digitizer or pipeline into a nonlinear regime. This saturation leads to a distinct peak in the time profile of the flagged samples, precisely coinciding with the burst location. These examples validate the effectiveness of our automated flagging routines in distinguishing between general RFI and instrumental saturation, ensuring the integrity of the burst profiles and measured parameters used in the catalog.

dynamic spectra. These points were then frequency integrated to generate time profiles. Two distinct scenarios were identified: time profiles showing uniform temporal distribution, which indicate noise or radio-frequency interference (RFI) effects (see Figure 9(a)), and time profiles matching the burst temporal structure, which signify genuine saturation (see Figure 9(b)). Bursts exhibiting the latter characteristic were excluded from subsequent analysis. It should be noted that the value 255 or 127 itself does not directly indicate saturation. The key criterion for identifying saturation is observing whether the distribution of tracers aligns with the pulse morphology. However, this serves only as an operational guideline, as the underlying principles are quite complex. Consequently, in practice there is no single unique method for determining saturation. Applying this methodology to the sample of bursts with $S/N \geqslant 20$ revealed 253 saturated events, which were subsequently removed to ensure reliable polarization measurements.

Appendix B
RM Synthesis

Due to the Faraday effect, the polarization plane of the FRB signal rotates during propagation. We employed the RM synthesis method to search for the RM of the burst by considering the equation of

$$\begin{pmatrix} I \\ Q' \\ U' \\ V \end{pmatrix} = \begin{pmatrix} 1 & 0 & 0 & 0 \\ 0 & \cos 2\theta & \sin 2\theta & 0 \\ 0 & -\sin 2\theta & \cos 2\theta & 0 \\ 0 & 0 & 0 & 1 \end{pmatrix} \begin{pmatrix} I \\ Q \\ U \\ V \end{pmatrix}, \tag{B1}$$

where $\theta = \mathrm{RM}\lambda^2$. In our implementation, the trial RM range is set to -2000 to $+2000$ rad m^{-2}. This interval was chosen as a conservative search range, substantially broader than the RMs measured for FRB 20240114A, while avoiding an unnecessarily wide search domain. The intrachannel depolarization factor can be written as $f_{\mathrm{depol}} = |\sin(\mathrm{RM}\Delta\lambda^2)/(\mathrm{RM}\Delta\lambda^2)|$, where $\Delta\lambda^2 \approx 2c^2\Delta\nu/\nu_c^3$ in the narrow-channel approximation (B. J. Burn 1966; M. A. Brentjens & A. G. de Bruyn 2005). For the present FAST L-band channelization ($\Delta\nu \approx 0.122$ MHz), 10% depolarization at the bottom of the band occurs only at $|\mathrm{RM}| \sim 1.8 \times 10^4$ rad m^{-2}, far above both our adopted search range and the RMs measured in this work. The RM uncertainty is estimated empirically from the width of the RM-synthesis peak. Specifically, after identifying the RM corresponding to the maximum of the RM spectrum, we determine the left and right peak widths using the points where the spectrum drops below the midpoint between its maximum and minimum values and divide these widths by the burst S/N. This yields asymmetric RM uncertainties when the RM-synthesis peak is not perfectly symmetric. For the present catalog, the RM analysis is restricted to bursts with $S/N \geqslant 20$, for which the RM-synthesis peak is in most cases visually well defined. In practice, the corresponding polarization and RM-synthesis diagnostic plots were also inspected to identify obviously spurious cases. A more formal calibration of peak significance could in principle be obtained through dedicated Monte Carlo simulations, but this is beyond the scope of the present catalog paper. In addition to the empirical

peak-width-based RM uncertainty quoted here, one RM-search grid step may be regarded as an additional systematic uncertainty ($\sim$0.2 rad m^{-2}) associated with the discretization of the RM search. Due to challenges in calculating RM from weak signals or bursts with narrow emission BWs, RM values were successfully measured for only 6131 of the detected bursts. The mean value of the RM is 359.52 rad m^{-2}, showing significant variations throughout the observing campaign, ranging from 212.50 rad m^{-2} to 420.50 rad m^{-2}. We corrected the Stokes components Q and U by derotating them using the measured RM. The degree of linear and circular polarization is calculated as

$$L/I = \frac{\Sigma_i L_i}{\Sigma_i I_i}, \quad V/I = \frac{\Sigma_i V_i}{\Sigma_i I_i}, \tag{B2}$$

where I_i and V_i are defined as the frequency-averaged total intensity and circular polarization measured for the time sample i, and $L_i = \sqrt{Q_i^2 + U_i^2}$ is the frequency-averaged total linear polarization measured for the time sample i, respectively. Due to the quadrature summation $L = \sqrt{Q^2 + U^2}$, the probability density function of L is non-Gaussian (see below). In addition, there exists a positive bias in the measured values at low L, which means the linear polarization can be subject to overestimation when noise is present. To remove the bias and calculate the true value of linear polarization, we employ the following equation to debias (J. E. Everett & J. M. Weisberg 2001):

$$L_{\rm de-bias} = \begin{cases} \sigma_I \sqrt{\left(\frac{L_i}{\sigma_I}\right)^2 - 1}, & \frac{L_i}{\sigma_I} > 1.57 \\ 0, & \frac{L_i}{\sigma_I} < 1.57 \end{cases}, \tag{B3}$$

where σ_I is the off-pulse standard deviation in Stokes parameter I.

For a subset of low-S/N bursts, the formally measured L/I can exceed 100% (see Figure 5). These cases are preferentially associated with bursts whose intrinsic linear polarization is already very high, i.e., close to complete linear polarization. In such events, off-pulse noise fluctuations can occasionally yield $L > I$ in the background, and when the burst itself has relatively low integrated S/N, the accumulated result can produce $\sum L > \sum I$. We therefore interpret these values not as physically meaningful super-100% polarization fractions, but as noise-biased measurements of bursts whose true L/I is likely close to 100%.

Appendix C
Correction for Ionospheric Faraday Rotation

The Earth's ionosphere contributes an additive, time-variable component to the observed RM. To quantify and remove this effect, we calculate the ionospheric RM for each observing session using Python code IonFR and GIM products. The GIM products are available on NASA's website[39] in the IONosphere EXchange (IONEX) format. The ionospheric RM as a function of time is presented in Figure 10. Throughout our entire observing campaign, the ionospheric RM has a mean value of 3.49 rad m^{-2} with a standard deviation of 1.06 rad m^{-2}. This contribution is over an order of magnitude smaller than the $\sim$200 rad m^{-2} intrinsic RM evolution we report for FRB 20240114A. More importantly, its temporal variability is negligible compared to the source intrinsic changes. Therefore, we conclude that the ionospheric contribution does not account for the observed dramatic RM evolution. All RM values presented in the final catalog have been corrected by subtracting the ionospheric RM for the corresponding MJD.

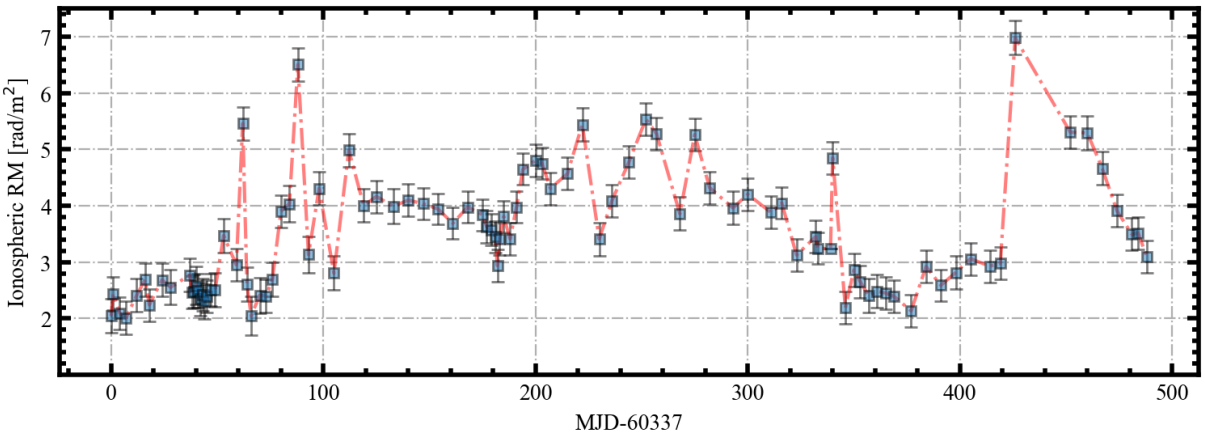


Figure 10. Contribution of the Earth's ionosphere to the observed rotation measure. The plot shows the ionospheric RM as a function of time. The mean ionospheric RM throughout the campaign is 3.49 $\pm$ 1.06 rad m^{-2}.

[39] http://cddis.nasa.gov/archive/gnss/products/ionex/

Appendix D
Energy Distance

Energy distance is a statistical metric that quantifies the discrepancy between two multivariate probability distributions. It operates directly on the moments of interpoint distances, offering a nonparametric and geometrically intuitive measure of distributional difference (G. Szekely & M. Rizzo 2004; G. J. Székely & M. L. Rizzo 2013a).

Definition. Let X and X' be independent and identically distributed (i.i.d.) random vectors from distribution P, and let Y and Y' be i.i.d. from distribution Q, all defined on $\mathbb{R}^d$ with finite first moments. The energy distance $\mathcal{D}_E(P, Q)$ is defined as (G. Szekely & M. Rizzo 2004; G. J. Székely & M. L. Rizzo 2013a)

$$\mathcal{D}_E(P, Q) = 2\,\mathbb{E}\|X - Y\| - \mathbb{E}\|X - X'\| - \mathbb{E}\|Y - Y'\|,$$

where $\mathbb{E}$ denotes the expectation and $\|\cdot\|$ is the Euclidean norm (or, more generally, a suitable metric).

Key properties. The energy distance satisfies the following essential properties (G. Szekely & M. Rizzo 2004; G. J. Székely & M. L. Rizzo 2013a, 2013b):

1. *Nonnegativity and identity*. $\mathcal{D}_E(P, Q) \geqslant 0$, and $\mathcal{D}_E(P, Q) = 0$ if and only if $P = Q$ almost everywhere. This makes it a proper statistical *distance* or *metric*.

2. *Equivalence via characteristic functions*. An alternative, powerful characterization links it to the characteristic functions $\phi_P(t)$ and $\phi_Q(t)$ of the distributions (G. Szekely & M. Rizzo 2004; G. J. Székely & M. L. Rizzo 2013a):

$$\mathcal{D}_E(P, Q) = \frac{1}{c_d}\int_{\mathbb{R}^d} \frac{|\phi_P(t) - \phi_Q(t)|^2}{\|t\|^{d+1}} dt,$$

where c_d is a dimensional constant. This formulation shows that $\mathcal{D}_E$ measures the weighted L^2 difference between the characteristic functions.

3. *Sample estimator*. Given empirical samples $\{x_i\}_{i=1}^n \sim P$ and $\{y_j\}_{j=1}^m \sim Q$, $\mathcal{D}_E$ can be estimated unbiasedly from interpoint distances, making it applicable to real-world data (G. J. Székely & M. L. Rizzo 2013a).

Applications. In statistical and machine learning contexts, energy distance is widely used for two-sample hypothesis testing (the *energy test*), assessing the convergence of generative models, and as a loss function in domain adaptation (G. Szekely & M. Rizzo 2004; G. J. Székely & M. L. Rizzo 2013a; D. Sejdinovic et al. 2013). Its primary advantages are its metric properties, sensitivity to all moments, and computational feasibility for moderate sample sizes.

Note. In the main text, we use the energy distance to quantify the difference between the joint distributions of the linear and circular polarization fractions of cumulative bursts in consecutive observing sessions over different timescales. Specifically, each burst is represented as a two-dimensional vector

$$\boldsymbol{x}_i = \left(\frac{L_i}{I_i}, \frac{V_i}{I_i}\right), \tag{D1}$$

where L_i/I_i and V_i/I_i denote the linear and circular polarization fractions, respectively. For two samples $X = \{\boldsymbol{x}_i\}_{i=1}^m$ and $Y = \{\boldsymbol{y}_j\}_{j=1}^n$ from two observing sessions, we compute the sample energy distance as

$$\mathcal{E}(X, Y) = \frac{2}{mn}\sum_{i=1}^{m}\sum_{j=1}^{n}\|\boldsymbol{x}_i - \boldsymbol{y}_j\| - \frac{1}{m^2}\sum_{i=1}^{m}\sum_{j=1}^{m}\|\boldsymbol{x}_i - \boldsymbol{x}_j\| - \frac{1}{n^2}\sum_{i=1}^{n}\sum_{j=1}^{n}\|\boldsymbol{y}_i - \boldsymbol{y}_j\|, \tag{D2}$$

where $\|\cdot\|$ is the Euclidean distance in the two-dimensional polarization-fraction space. A larger value of $\mathcal{E}$ indicates a greater discrepancy between the two joint distributions.

ORCID iDs

Tian-Cong Wang https://orcid.org/0000-0002-9332-5562
Jun-Shuo Zhang https://orcid.org/0009-0005-8586-3001
Xiao-Hui Liu https://orcid.org/0000-0002-2552-7277
Wei-Yang Wang https://orcid.org/0000-0001-9036-8543
Pei Wang https://orcid.org/0000-0002-3386-7159
He Gao https://orcid.org/0000-0003-2516-6288
Di Li https://orcid.org/0000-0003-3010-7661
Bing Zhang https://orcid.org/0000-0002-9725-2524
Wei-Wei Zhu https://orcid.org/0000-0001-5105-4058
Ye Li https://orcid.org/0000-0001-5931-2381
Dengke Zhou https://orcid.org/0000-0002-7420-9988
Jintao Xie https://orcid.org/0000-0001-5649-2591
Jianhua Fang https://orcid.org/0000-0001-9956-6298
Yunchuan Chen https://orcid.org/0009-0000-4795-8767
Huaxi Chen https://orcid.org/0009-0000-6108-2730
Qin Wu https://orcid.org/0000-0001-6021-5933
Long-Xuan Zhang https://orcid.org/0009-0002-3020-9123
Yong-Kun Zhang https://orcid.org/0000-0002-8744-3546
De-Jiang Zhou https://orcid.org/0000-0002-6423-6106
Jia-Rui Niu https://orcid.org/0000-0001-8065-4191
Xuelei Chen https://orcid.org/0000-0001-6475-8863
Yuan-Pei Yang https://orcid.org/0000-0001-6374-8313
Fa-Yin Wang https://orcid.org/0000-0003-4157-7714
Chao-Wei Tsai https://orcid.org/0000-0002-9390-9672
Wen-Fei Yu https://orcid.org/0000-0002-3844-9677
Chen-Hui Niu https://orcid.org/0000-0001-6651-7799
Jia-Wei Luo https://orcid.org/0000-0002-9642-9682
Rui Luo https://orcid.org/0000-0002-4300-121X
Zi-Wei Wu https://orcid.org/0000-0002-1381-7859
Chun-Feng Zhang https://orcid.org/0000-0002-4327-711X
Xiang-Lei Chen https://orcid.org/0000-0001-5738-9625
Shuai Feng https://orcid.org/0009-0006-0803-0505
Xiang-Han Cui https://orcid.org/0000-0002-6165-0977
Yuan-Hong Qu https://orcid.org/0000-0003-4721-4869
Bo-Jun Wang https://orcid.org/0000-0002-9434-4773
Lin Lin https://orcid.org/0000-0002-0633-5325
Yuan-Chuan Zou https://orcid.org/0000-0002-5400-3261
Wei-Cong Jing https://orcid.org/0000-0002-1056-5895
Jian Li https://orcid.org/0000-0003-1720-9727
Yong-Feng Huang https://orcid.org/0000-0001-7199-2906
Su-Ming Weng https://orcid.org/0000-0001-7746-9462
Shi-Han Yew https://orcid.org/0000-0002-5799-9869
Xue-Feng Wu https://orcid.org/0000-0002-6299-1263
Lei Zhang https://orcid.org/0000-0001-8539-4237
Ru-Shuang Zhao https://orcid.org/0000-0002-1243-0476

References

Anna-Thomas, R., Connor, L., Dai, S., et al. 2023, Sci, 380, 599
Astropy Collaboration, Robitaille, T. P., Tollerud, E. J., et al. 2013, A&A, 558, A33
Bethapudi, S., Li, D. Z., Spitler, L. G., et al. 2025, A&A, 702, A248
Brentjens, M. A., & de Bruyn, A. G. 2005, A&A, 441, 1217
Burn, B. J. 1966, MNRAS, 133, 67
CHIME/FRB Collaboration, Amiri, M., Bandura, K., et al. 2019, Natur, 566, 235
CHIME/FRB Collaboration, Amiri, M., Andersen, B. C., et al. 2020, Natur, 582, 351
Everett, J. E., & Weisberg, J. M. 2001, ApJ, 553, 341
Feng, Y., Li, D., Yang, Y.-P., et al. 2022b, Sci, 375, 1266
Feng, Y., Zhang, Y.-K., Li, D., et al. 2022a, SciBu, 67, 2398
Feng, Y., Zhang, Y.-K., Xie, J., et al. 2025, SCPMA, 68, 289511
Feng, Y., Zhou, D., Zhang, Y.-K., et al. 2026, arXiv:2604.01825
Hilmarsson, G. H., Michilli, D., Spitler, L. G., et al. 2021, ApJL, 908, L10
Hotan, A. W., van Straten, W., & Manchester, R. N. 2004, PASA, 21, 302
Hutschenreuter, S., Anderson, C. S., Betti, S., et al. 2022, A&A, 657, A43
Jiang, J.-C., Wang, W.-Y., Xu, H., et al. 2022, RAA, 22, 124003
Jiang, J. C., Xu, J. W., Niu, J. R., et al. 2024, NSRev, 12, nwae293
Li, D., Wang, P., Zhu, W. W., et al. 2021, Natur, 598, 267
Li, Y., Zhang, S. B., Yang, Y. P., et al. 2026, Sci, 391, 280
Lin, H.-H., Main, R., Pen, U.-L., et al. 2022, arXiv:2208.13677
Liu, X., Xu, H., Niu, J., et al. 2025, ApJ, 988, 175
Lorimer, D. R., Bailes, M., McLaughlin, M. A., Narkevic, D. J., & Crawford, F. 2007, Sci, 318, 777
Luo, R., Wang, B. J., Men, Y. P., et al. 2020, Natur, 586, 693
Mckinven, R., Gaensler, B. M., Michilli, D., et al. 2023a, ApJ, 951, 82
Mckinven, R., Gaensler, B. M., Michilli, D., et al. 2023b, ApJ, 950, 12
Michilli, D., Seymour, A., Hessels, J. W. T., et al. 2018, Natur, 553, 182
Moroianu, A. M., Bhandari, S., Drout, M. R., et al. 2026, ApJL, 996, L16
Nan, R., Li, D., Jin, C., et al. 2011, IJMPD, 20, 989
Ng, C., Pandhi, A., Mckinven, R., et al. 2025, ApJ, 982, 154
Niu, C.-H., Aggarwal, K., Li, D., et al. 2022, Natur, 606, 873
Niu, J. R., Wang, W. Y., Jiang, J. C., et al. 2024, ApJL, 972, L20
Ocker, S. K., & Cordes, J. M. 2026, ApJ, 1002, 3
Ould-Boukattine, O. S., Cooper, A. J., Hessels, J. W. T., et al. 2026, MNRAS, 546, stag090
Panda, U., Roy, J., Bhattacharyya, S., Dudeja, C., & Kudale, S. 2025, ApJ, 989, 15
Pandhi, A., Pleunis, Z., Mckinven, R., et al. 2024, ApJ, 968, 50
Pandhi, A., Nimmo, K., Andrew, S., et al. 2026, ApJL, 1000, L53
Qu, Y., & Zhang, B. 2023, MNRAS, 522, 2448
Ransom, S. M. 2001, AAS Meeting, 199, 119.03
Scott, D. R., Dial, T., Bera, A., et al. 2025, PASA, 42, e133
Sejdinovic, D., Sriperumbudur, B., Gretton, A., & Fukumizu, K. 2013, AnSta, 41, 2263
Sherman, M. B., Connor, L., Ravi, V., et al. 2024, ApJ, 964, 131
Shin, K., Curtin, A., Fine, M., et al. 2026, ApJ, 997, 334
Sotomayor-Beltran, C., Sobey, C., Hessels, J. W. T., et al. 2013, ionFR: Ionospheric Faraday rotation, Astrophysics Source Code Library, ascl:1303.022
Spitler, L. G., Scholz, P., Hessels, J. W. T., et al. 2016, Natur, 531, 202
Szekely, G., & Rizzo, M. 2004, InterStat, 5, 1249
Székely, G. J., & Rizzo, M. L. 2013a, J. Stat. Plan. Inference, 143, 1249
Székely, G. J., & Rizzo, M. L. 2013b, J. Multivar. Anal., 117, 193
Thornton, D., Stappers, B., Bailes, M., et al. 2013, Sci, 341, 53
Tian, J., Rajwade, K. M., Pastor-Marazuela, I., et al. 2024, MNRAS, 533, 3174
Uttarkar, P. A., Shannon, R. M., Lower, M. E., et al. 2024, MNRAS, 534, 2485
Uttarkar, P. A., Shannon, R. M., Gourdji, K., et al. 2026a, arXiv:2602.16409
Uttarkar, P. A., Shannon, R. M., Gourdji, K., et al. 2026b, MNRAS, 545, staf1997
Virtanen, P., Gommers, R., Oliphant, T. E., et al. 2020, NatMe, 17, 261
Wang, F. Y., Zhang, G. Q., Dai, Z. G., & Cheng, K. S. 2022, NatCo, 13, 4382
Wang, P., Zhang, J. S., Yang, Y. P., et al. 2025, arXiv:2507.15790
Wang, P., Li, J., Ji, L., et al. 2024, ApJS, 275, 39
Wang, W.-Y., Liu, X., Li, D., et al. 2025, ApJ, 988, 164
Xie, J.-T., Feng, Y., Li, D., et al. 2025, ApJS, 278, 49
Xu, H., Niu, J. R., Chen, P., et al. 2022, Natur, 609, 685
Yamasaki, S., & Totani, T. 2020, ApJ, 888, 105
Yang, Y.-P., Li, Q.-C., & Zhang, B. 2020, ApJ, 895, 7
Yang, Y.-P., Xu, S., & Zhang, B. 2023, MNRAS, 520, 2039
Yao, J. M., Manchester, R. N., & Wang, N. 2017, ApJ, 835, 29
Zhang, B. 2023, RvMP, 95, 035005
Zhang, J.-S., Wang, T.-C., Wang, P., et al. 2025, arXiv:2507.14707
Zhang, L.-X., Tian, S., Shen, J., et al. 2025, ApJ, 998, 276
Zhang, Y.-K., Li, D., Feng, Y., et al. 2025, ApJS, 276, 20
Zhang, Y.-K., Li, D., Zhang, B., et al. 2023, ApJ, 955, 142
Zhou, D., Han, J. L., Zhang, B., et al. 2025, ApJ, 988, 41
Zhou, D., Wang, P., Fang, J., et al. 2026, SCPMA, 69, 249512